ABSTRACT

Title of Thesis: GROWTH OF HEXAGONAL BORON NITRIDE ON ELECTROCHEMICALLY PREPARED POLYCRYSTALLINE COPPER SUBSTRATES

Karthik Sridhara, Master of Science, 2014

Thesis directed by: Dr. D. Kurt Gaskill
Naval Research Laboratory, Washington DC

Prof. Michael S. Fuhrer
Department of Physics, University of Maryland
College Park, MD
&
School of Physics
Monash University, Australia

The growth of two dimensional materials such as graphene and hexagonal boron nitride (h-BN) have been demonstrated by chemical vapor deposition (CVD) on polycrystalline copper catalytic substrates. Polycrystalline copper foil substrates most often utilized in CVD approaches are produced by metallurgical rolling, a technique which forms irregular ridges on the foil surface and can introduce contaminants. The Cu foil supplied by vendors, such as Sigma Aldrich or Alfa Aesar, also has a film of native oxide on the surface. These processing artifacts, irregular ridges, along with the native oxide are a limiting factor for controlled and reproducible large area (several cm^2) growth of these low-dimensional materials envisaged to be used for microelectronics. Greater control of growth can be achieved by con-

trolling the density of nucleation sites and improving the catalytic activity of Cu by removing the native oxide on the Cu surface. Previous attempts to pre-treat the Cu substrate either by using wet chemistry and thermal annealing to control growth has been weakly addressed.

In this work, electrochemical polishing (electropolishing) combined with prior thermal annealing at 1030°C for 5 hours under H_2-N_2 is used to control the degree of roughness of cold rolled polycrystalline Cu foils, and subsequently, to explore the influence of electropolishing on the growth of h-BN. Electropolishing dissolves a thin surface layer of copper, which contains surface defects and contaminants. This helps in decreasing the density of spontaneous nucleation sites by producing a morphologically uniform and contaminant-free surface. Secondary effects during electropolishing, such as etch pits, arise from the standard electropolishing recipe of concentrated H_3PO_4. These secondary effects, ascribed to oxygen bubbling at random nucleation sites on Cu surface, can be overcome by using additives, such as acetic acid and ethylene glycol, as oxygen suppressors in the electrolyte to counter formation of etch pits and to prepare a planarized substrate. The additives are added to the standard electrolyte with a volume ratio of 25% Ethylene Glycol, 25% Acetic Acid, 50% concentrated H_3PO_4 forming a compound electrolyte and a potential of 2.3 V is applied for 30 minutes for electropolishing to occur. Atomic Force Microscopy (AFM) reveals that a roughness of ≈ 1.2 nm (R_q) and a greatly planarized Cu foil without the waviness from metallurgical rolling can be achieved with the two step: thermal annealing followed by two-additive electropolishing process. Fourier Transform Infrared (FTIR) spectroscopy is used to confirm the existence of h-BN

on electropolished substrates. Subsequent growth studies of h-BN on high quality copper substrates demonstrate improved growth, as demonstrated by the metrics of size and count of h-BN crystals from Scanning Electron Microscopy (SEM) micrographs. The work proves that thermal annealing followed by electropolishing leads to optimization of copper foil surface resulting in the larger crystal size of h-BN and reduction in nucleation sites that induce h-BN crystal growth. AFM is also used to establish the Cu substrate morphology and its relationship to the growth of h-BN crystals.

Growth of hexagonal boron nitride on electrochemically prepared polycrystalline copper substrates

by

Karthik Sridhara

Thesis submitted to the Faculty of the Graduate School of the
University of Maryland, College Park in partial fulfillment
of the requirements for the degree of
Master of Science
2014

Advisory Committee:
Assoc. Prof. John Cumings, Chair
Dr. D. Kurt Gaskill, Advisor
Prof. Michael S. Fuhrer
Prof. Manfred Wuttig
Dr. Karen Gaskell

Dedication

This work is dedicated to my parents and my brother.

Acknowledgments

I owe my gratitude to all the people who have made this work possible.

First and foremost I'd like to thank my advisor, Professor John Cumings at University of Maryland for the academic guidance.

I would also like to thank my research supervisors: Dr. D. Kurt Gaskill (co-PI) at the U.S. Naval Research Laboratory (NRL) and Prof. Michael Fuhrer at UMD Physics (now at Monash University, Aus) for research guidance throughout my time at NRL and UMD. I am deeply thankful for their guidance and their high expectations. I would also like to thank my committee members: Prof. Manfred Wuttig and Dr. Karen Gaskell for being on committee.

I would also like to thank my supervisor and the other co-PI for this work at NRL, Dr. Boris Feigelson. I first saw him when I was 14 years old on BBC documentary on diamond growth, which inspired me to pursue material science. I consider it a personal honor to work under his supervision. I have learnt a great deal, not just about performing scientific experiments but also to think like a scientist. It has been a pleasure to work with him and learn from such an extraordinary individual. Special thanks to Dr. James A. Wollmershauser at NRL for his invaluable support and guidance on writing this thesis. I would also like to acknowledge Dr. Derek Horton and Dr. Sandra Hernandez-Hangarter for the support and guidance on electropolishing experiments and discussions on electrochemistry. Dr. Paul Klein at NRL for guidance on the thesis defense presentation. Anindya Nath and Dr. Jennifer Hite for SEM micrographs of samples.

I owe my deepest thanks to my family: my parents and my brother, and my friends: Laleh Emdadi and Nikhil Ahuja, who have always stood by me and supported my endeavors.

I would like to acknowledge financial support from the Office of Naval Research (ONR) for the work discussed herein.

Table of Contents

1 Introduction **1**
- 1.1 Background . . . 2
- 1.2 Growth of graphene and h-BN using CVD . . . 5
- 1.3 Morphology of vendor supplied Cu foil . . . 7

2 Electropolishing: Theory and Practice **12**
- 2.1 Electrochemistry . . . 12
- 2.2 The theory and practice of electropolishing . . . 13
- 2.3 Progression of methods for this work . . . 18
  - 2.3.1 Method A . . . 18
  - 2.3.2 Method B . . . 22
  - 2.3.3 Method C . . . 29
  - 2.3.4 Experimental Plan . . . 30
- 2.4 Characterization Techniques . . . 32

3 Results and discussion of Cu electropolishing and surface evolution **34**
- 3.1 Electropolishing of Cu anode . . . 35
- 3.2 Surface morphology of Cu: Before and after thermal annealing . . . 37
- 3.3 Cu surface evolution after thermal anneal and electropolishing . . . 42
- 3.4 Electropolishing using the two-additive process . . . 47

4 Growth of hexagonal boron nitride on electropolished Cu foils **55**
- 4.1 Growth of h-BN . . . 56
  - 4.1.1 h-BN on non-additive electropolished Cu . . . 56
  - 4.1.2 h-BN on two-additive electropolished Cu . . . 59
- 4.2 Surface morphology of h-BN on Cu surface . . . 63
  - 4.2.1 Morphology of h-BN on Cu TA-2 . . . 66
  - 4.2.2 Morphology of h-BN on Cu TA EP-2 . . . 67

5 Summary and conclusions **70**

6 Future work **72**

Bibliography **73**

List of Figures

1.1 Graphene (a) and its analog, hexagonal boron nitride (b). In a, the black ball shown represents carbon. In b) the purple and the grey ball represents nitrogen and boron, respectively. 4
1.2 Metallurgical rolling of Cu. a) Two dimensional representation of the cold rolling process. b) Two dimensional view of Cu foils after cold rolling process. c) Three dimensional representation of the cold rolling process. Figure redrawn from [5, 6]. 8
1.3 Evolution of Cu surface before and after thermal annealing under H_2 gas environment. a) Grain enlargement after thermal annealing. b) Removal of native oxide from the Cu surface. c) Surface normalization by smoothing high asperities. 10
1.4 Impact of thermal annealing on Cu. a) Step edges become prominent. b) Contaminants from the bulk diffuse on to the surface. The diffusion direction is indicated by arrows. 11

2.1 A simple electrochemical cell. The two electrodes: counter (Pt) and working electrode (Cu) is shown along with the electrolyte. 13
2.2 Current-Voltage relationship in an electrochemical cell for Cu electropolishing. The three regions: etching, dissolution and oxygen evolution is marked as A, B and C in the figure. Figure redrawn from [60]. The target voltage, also called inflection voltage due to transition from dissolution to oxygen evolution region, is indicated with a blue dot. 15
2.3 Formation of viscous layer at the electrode and the concentration gradient at the surface asperities. 17
2.4 Electropolishing setup for Method A. Power supply: Agilent E3640 DC power supply, HP/Agilent 34405A multimeter as ammeter, and Fluke 170 series multimeter as voltmeter. 20
2.5 Experimental setup of the electrolytic cell for Method A. 21
2.6 Experimental setup of the electrolytic cell for Method B. 23
2.7 Tearing of the Cu sample during the electropolishing process beyond 30 minutes. The point where the Cu sample is torn due to significant thinning is indicated with the arrow. 26
2.8 An example of etch pits (large ones) that occur with standard (concentrated H_3PO_4) electropolishing. The diameter of the etch pits are ≈ 100 μm. 28

2.9 Cyclic voltammetry and chronoamperometry (limiting current) of electropolishing performed in concentrated (85% concentrated) H_3PO_4 in a and b, respectively. The increase in current observed from reusing the electrolyte is indicated in a and b. 31

3.1 Cyclic voltammetry and chronoamperometry (limiting current) of electropolishing performed in concentrated H_3PO_4 in a and b, respectively. The increase in current observed from reusing the electrolyte is indicated in a and b. 36
3.2 Optical (above) and Nomarski (below) images of Cu (a, b) and Cu TA (d, e) under the microscope (5x magnification). SEM images shown in c and f are a localized view of the Cu and Cu TA surfaces, respectively. The direction of rolling lines are indicated in Cu and Cu TA, a and d, respectively. The Cu grain, which enlarges and becomes more visible after thermal annealing, is indicated using the red dashed circle. The scale bar is 200 μm for optical images and 2 μm for SEM images. 38
3.3 A 10 μm × 10 μm tapping mode atomic force microscopy profile of Cu before and after thermal annealing, a and b respectively. c and d show the histogram of height and phase distribution of Cu data before and after annealing (indicated). 39
3.4 Tapping mode AFM of Cu TA surface with, a) height, and b) phase image. c) A line scan of a potential nucleation site is also shown as an example. d) SEM image of Cu TA. The potential nucleation sites are clearly visible and marked on both the AFM and SEM images. . 42
3.5 Optical and Nomarski images of surface morphology evolution of Cu before and after thermal annealing and evolution of Cu TA with the duration of electropolishing time: 15, 30 and 45 minutes (c, d and e, respectively). f) Example of etch pits forming on the Cu surface during electropolishing. 44
3.6 High resolution X-Ray Photoelectron Spectroscopy of Cu 2p. The inset shows the relative composition of Cu and O on the surface. The XPS signal associated with the thinning of native oxide (shown using an arrow) below the XPS detection limit after Cu thermal annealing and electropolishing of thermally annealed Cu sample. 46
3.7 Voltammetry of various additives in standard electrolyte (concentrated H_3PO_4). The addition of additives reduces the current when contrasted with concentrated electrolyte indicated using a dashed curve. 48
3.8 Tapping mode AFM height and phase images of Cu TA EP-2 (a and b, respectively) and Cu EP-2 (c and d, respectively) with the two additive electropolishing. 50
3.9 Average RMS roughness evolution after each processing step of Cu surface. Electropolishing decreases the roughness after thermal annealing but reaches a plateau. The red square shows the data point of average RMS roughness of Cu TA EP-2. 52

3.10 Line profiles of AFM height image of Cu TA EP-2 shown in a) and b). The RMS roughness measured across the whole 10 μm × 10 μm scan is ≈ 1.1 nm. 53
3.11 SEM images of Cu TA with standard electropolishing and two-additive electropolishing. a and b are Cu samples without and with thermal annealing electropolished using the standard non-additive electropolishing. c and d are Cu samples without and with thermal annealing using the two additive electropolishing process. The scale bar is 400 μm and the magnification is 22x. 54

4.1 SEM images of h-BN grown on thermally annealed Cu foil (control sample) and electropolished Cu foil. The dashed outline shows the h-BN crystals and the bright dot-like structures are the nucleation sites. 58
4.2 Attenuated Total Reflectance Fourier Transform Infrared (ATR-FTIR) spectroscopy of thermally annealed Cu and electropolished Cu using the standard electrolyte. 59
4.3 SEM of h-BN crystals grown on a) electropolished Cu (Cu EP-2) and b) thermally annealed electropolished Cu (Cu TA EP-2) and c) thermally annealed Cu TA-2. The h-BN crystals are indicated by triangular outline in a, b, and c. h-BN crystals merging is indicated in a) and b). The red dashed square shows crystal merging in c). The red dashed line in a) shows the location of Cu grain boundaries. . . . 61
4.4 ATR-FTIR of h-BN on Cu TA EP-2, Cu EP-2 and Cu TA (top to bottom). 63
4.5 Tapping mode AFM of h-BN on Cu TA (top) and Cu TA EP-2 (bottom). a) and c) are height images of Cu TA and Cu TA EP-2, respectively and b) and d) are phase images of Cu TA and Cu TA EP-2, respectively. The AFM scan size in 20 μm × 20 μm. The blue dashed squares are 5 μm × 5 μm AFM scans shown in Figure 4.6 and Figure 4.7. The dashed yellow oval indicated in c) shows the hump-like oblique protruding feature on Cu TA EP-2 surface is ≈ 1 μm wide and ≈ 3 μm long. 65
4.6 A 5μm × 5 μm AFM scan of h-BN on Cu TA. A) Height, b) Phase. Line scan of the nucleation site in a) is shown in c). 67
4.7 AFM surface morphology of h-BN on Cu TA EP-2. a) Height, b) Phase. Line scan of nucleation site and thickness of h-BN crystal shown as an example in c) and d), respectively. 1) and 2) on a) indicate the location from where the line scan is obtained. The lines drawn in d show the approximate region where the h-BN thickness is calculated. AFM scan size is 5 μm × 5 μm. 69

CHAPTER 1

Introduction

The goal of this work is to utilize electrochemical polishing to prepare smooth polycrystalline copper foils for the chemical vapor deposition (CVD) growth of hexagonal boron nitride (h-BN). In general, the approach involves developing an electrochemical polishing recipe for polycrystalline copper foils that modifies the surface morphology suitable for controllable CVD growth. Previous studies on CVD growth of h-BN and graphene on electropolished Cu foils have indicated that electropolishing alters the copper surface morphology improving growth of h-BN and graphene thin films [1, 2, 3, 4]. However, previous studies on electropolishing of Cu for CVD growth [1, 2, 3, 4] do not quantitatively assess the degree of improvement of the Cu surface such as roughness, nor develop a relationship between surface morphological preparation and controllable growth of h-BN and graphene, a necessity for controlled CVD growth. Polycrystalline copper foil used for growth of h-BN and graphene is prepared by metallurgical cold rolling and has a very rough surface with grooves and metal contaminants [5, 6, 7]. Consistent and uniform growth of 2D materials

requires a flat, contaminant-free surface [8, 9, 10, 11] and, therefore, the unaltered Cu foil surface as received from the vendor largely deviates from the ideal substrate free of surface defects, dramatically influencing growth. This work utilizes two-step thermal annealing and electropolishing to create a Cu foil surface that is laterally smooth with large Cu grains, reducing surface abnormalities and defects, and the density of nucleation sites. Roughness measurements are carried out to quantitatively assess the degree of improvement of Cu surface after each processing step. A relationship between the Cu surface morphology and the growth of h-BN will be assessed.

Electropolishing, a controlled dissolution of metal in an electrolyte with an applied potential, is chosen because of its simplicity, speed, versatility and ability to create a surface nearly free of defects [12]. Electropolishing has a simple setup as it requires four elements: a counter electrode, working electrode, an electrolyte and a potentiostat. Electropolishing is quick to use because the electropolishing operation takes only 15-30 minutes. Electropolishing can be applied on variety of surfaces to remove both macroscopic (> 1 μm) and microscopic (< 1 μm) surface features concurrently. It also has an ability to create a surface mostly free from deformations and surface defects [12].

1.1 Background

Graphene, a single atomically thick sheet of sp^2 hybridized graphitic carbon, has been envisaged to be used for various electronic applications, such as sensing of in-

dividual molecules [13, 14], integrated circuits [15, 16], transparent conducting electrode [17, 18], because of its unique electronic properties [16]. Considerable research efforts have been devoted to utilize graphene for microelectronic applications replacing silicon (≈ 1600 cm^2·V^{-1}·s^{-1}) [16, 19], due to graphene's high electron mobility ($> 100,000$ cm^2·V^{-1}·s^{-1}) [16, 20]. In order to fully utilize graphene for microelectronic applications, a gate dielectric is necessary. Silicon, the traditional material in microelectronic devices, has a native oxide SiO_2 that readily serves as a gate dielectric and is crystallographically compatible with Si. Graphene does not have such a luxury and very few materials are compatible with its hexagonal lattice structure and a small lattice coefficient. The choice of dielectric material should also fulfill two basic criteria as a substrate for graphene: 1) minimal interference with its electronic mobility and 2) structural compatibility i.e. a van der Waals surface with no dangling bonds. Hexagonal boron-nitride (h-BN), is the only known material available with a lattice constant of 1.44 Å, which is within 1.8% of graphene's 1.42 Å, and with a hexagonal lattice with sp^2 hybridization [21, 22]. More importantly, h-BN is also an insulator (or a wide band-gap semiconductor) with a band gap of 5.9 eV [21], which can also act as a gate and a tunneling dielectric [23, 24, 25, 26]. Figure 1.1 shows crystallographic structures of graphene and hexagonal boron nitride.

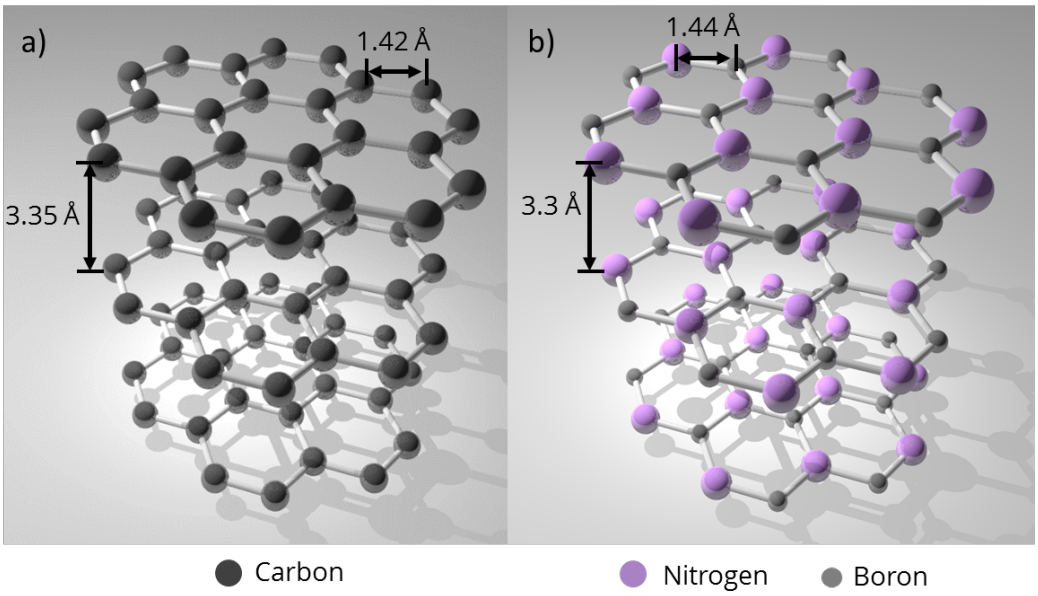

Figure 1.1: Graphene (a) and its analog, hexagonal boron nitride (b). In a, the black ball shown represents carbon. In b) the purple and the grey ball represents nitrogen and boron, respectively.

Graphene, with its two dimensional state, is expected to take the shape of the substrate on to which it is deposited [27]. Therefore, the surface morphology of the substrate plays a critical role in exploiting graphene's electronic properties to its fullest. h-BN has a very low surface roughness and preliminary studies show that graphene transferred on h-BN substrate (few atomic layers) has lower surface roughness than on SiO_2 [22]. As an extension to h-BN's capacity as an excellent substrate, monolayer h-BN is also shown to be an ideal candidate as a tunnel dielectric for graphene heterostructure applications [24]. However, these initial studies utilize h-BN crystals mechanically exfoliated from h-BN single crystals grown using a high temperature high pressure process [21] and transferred onto SiO_2 using a support

polymer (Poly(methyl methacrylate), PMMA) which may mean that it is sufficient for fundamental studies but not large area growth. Therefore, if graphene ever has to succeed in mainstream microelectronic applications, it would require h-BN to be grown on large areas.

1.2 Growth of graphene and h-BN using CVD

Mechanical exfoliation of graphene has been reported to exhibit the best electronic properties (highest electron mobility) and structural integrity (strongest material ever known) [28, 29]. However, mechanical exfoliation can produce up to 100 μm^2 areas of graphene [16,28]. While this is sufficient for fundamental studies of material properties, commercialization requires larger area growth (300 mm wafer size). High quality wafer scale (50 mm) graphene has been epitaxially grown on SiC through sublimation of silicon at high temperatures (1450°C) [30]. However, graphene grown on SiC suffers from a stepped surface that can limit device performance by scattering charge carriers flowing in the active graphene layer [31].Graphene is shown to be growing on polycrystalline Cu despite the existence of monatomic steps on the Cu surface [32]. Commercial applications of graphene demand economically viable techniques, such as CVD, for production of large areas, along with controllable, reproducible growth.

Chemical Vapor Deposition (CVD) has been utilized for the growth of oxides, and dielectric materials in large volume semiconductor manufacturing. CVD is a thin film deposition technique where precursors in vapor form are injected into a

reactor which is at high temperature ($> 700°C$). The precursors react chemically at the surface of the substrate leading to growth of solid material on the substrate. By-products are outgassed and exit the reactor in gaseous form. It is important that the injected precursors are volatile (gaseous) [33, 34].

CVD growth of graphene has been successfully achieved on polycrystalline copper substrates [35]. CVD growth of graphene has also been demonstrated on other transition metal elements including, Ni [18], Pd [36], Ru [37], Ir [38]. Single crystal copper has also been used [39] as a substrate, however with high cost and limited availability, single crystal copper is not considered as a viable substrate for mass production applications. On the other hand, polycrystalline copper is widely available, economical and high purity (up to 99.9999% purity) copper foils are available. Graphene primarily grows on Cu surface where the Cu atoms act as catalyst decomposing hydrocarbons (commonly from methane) at high temperature (around 1000°C) [35]. With hydrogen escaping as gas, the carbon atoms rearrange themselves forming an sp^2 lattice structure. The hexagonal lattice rearrangement takes place at nucleation sites and the growth propagates laterally eventually covering the entire copper substrate [35]. As carbon has extremely low solubility in Cu, Cu becomes very attractive for the growth of graphene [35].

Like graphene, hexagonal boron nitride has been shown to grow on polycrystalline copper and a variety of transition metal elements: Cu [4,40], Ni [41,42,43,44], Pd [45], Ru [46], and the underlying principle for growth is essentially the same as graphene. There are two precursors commonly used: ammonia borane (H_3NBH_3) [40] and borazine ($B_3H_6N_3$) [4]. With polycrystalline Cu acting as a catalyst and

a substrate, the surface morphology is critical for the lateral growth of h-BN and graphene. As h-BN, a graphene analog, has not been as thoroughly studied as graphene, any substrate induced effects on CVD growth reported for graphene will also apply to h-BN. Common surface morphological defects such as step edges and grain boundaries that appear in polycrystalline Cu substrates act as nucleation sites due to their high surface energy [47]. Therefore, it is important to discuss the surface morphological state of polycrystalline Cu and previous work done by other research groups to modify the surface morphology for improving the growth of graphene.

1.3 Morphology of vendor supplied Cu foil

High-purity (99.9998%) polycrystalline copper foils supplied by vendors such as Alfa Aeser is too rough ($>$ 100 nm in RMS roughness), and is susceptible to surface morphological defects in the form of rolling lines, arising from its preparation by metallurgical cold rolling as shown in Figure 1.2 [5,6,7]. The Cu surface is expected to contain native oxide (a combination of CuO and Cu_2O) which limits the catalytic nature of Cu [47, 48]. The grain size of Cu is also relatively small ($\approx$ 10 μm) and optically invisible [11]. The surface is also expected to be contaminated with other metals (like aluminum) during processing [5,6]. These morphological issues have a direct impact on the growth of h-BN and graphene by limiting the lateral growth. Surface defects such as grain boundaries and step edges act as nucleation sites. These nucleation sites assist adjacent crystallites to merge into each other during growth [9]. This hampers any attempt of continuous lateral growth of h-BN and

graphene crystals without merging into adjacent crystals.

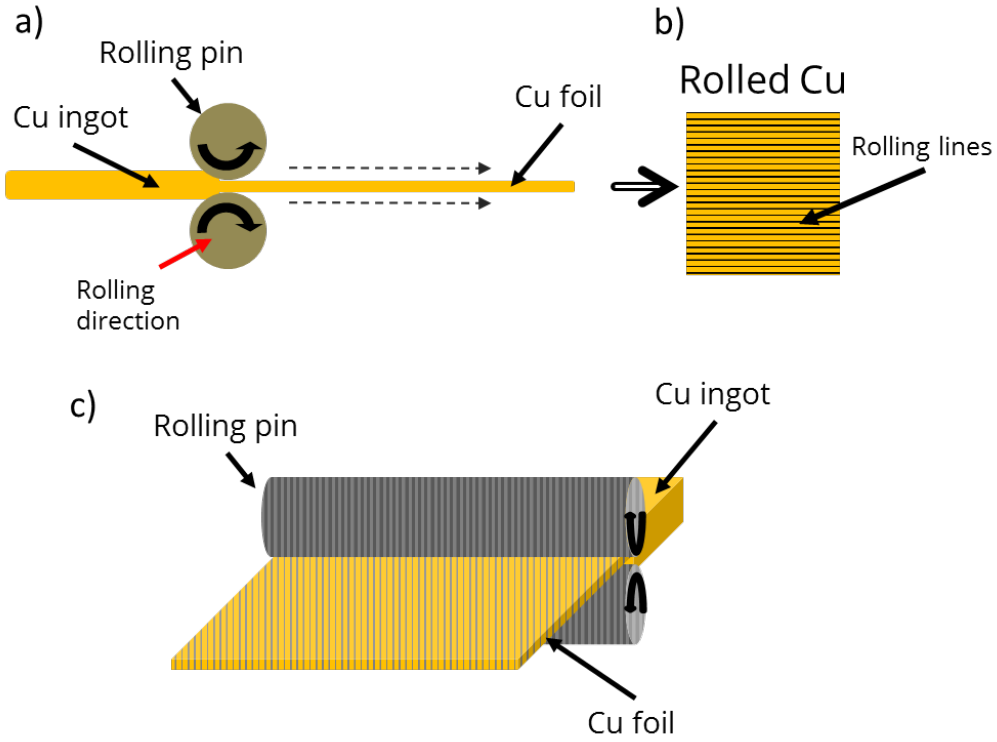

Figure 1.2: Metallurgical rolling of Cu. a) Two dimensional representation of the cold rolling process. b) Two dimensional view of Cu foils after cold rolling process. c) Three dimensional representation of the cold rolling process. Figure redrawn from [5, 6].

Reports have shown that pre-treatment of copper is critical if large area graphene growth is desired [47]. One of the pre-treatment techniques employed is to dip Cu in acetic acid [49] or nitric acid to remove the oxide [11]. However, these dipping techniques in acids are known to leave residues and etch quarries [11] negating any positive effect of oxide removal on the surface by these acids. Thermal annealing of Cu in a reducing environment is another technique that has gained

prominence due to its ability to recrystallize Cu grains by enlarging them and to remove native oxide [11,50,51,52,53,54,55] making the Cu surface more suitable for large area CVD growth. The larger grain size aids in uninterrupted lateral growth of h-BN and graphene, while the native oxide removal improves the catalytic nature of the Cu surface [47].

Thermal annealing in a reducing environment is shown to enlarge grains by recrystallizing several neighboring grains into a larger grain (Figure 1.3a) [50,51,56], while also removing the native oxide (Figure 1.3b) [53, 54, 55] of Cu, smoothing the surface as in Figure 1.3c. However, thermal annealing also has the following impacts on the Cu surface (also shown in Figure 1.4). Surface defects such as step edges become more prominent after thermal annealing [57]. Thermal annealing also does not lead to flattening of the substrate (discussed in chapter 3) but the high regions of the irregularities on the Cu surface become less prominent during the recrystallization process leading to a pseudo-smoothing effect. Despite the availability of high purity of polycrystalline Cu (99.999%, Sigma Aldrich), contaminants are present in low quantities ($\approx$ 300 ppm Sigma Aldrich) deep in the bulk and can diffuse onto the surface impacting the density of nucleation sites.

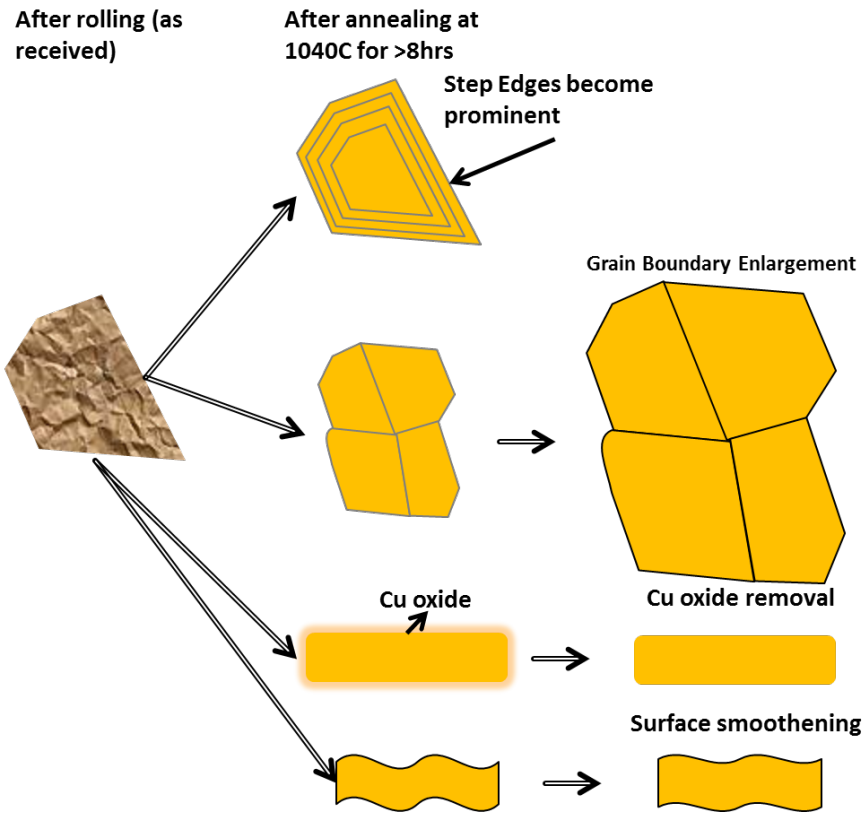

Figure 1.3: Evolution of Cu surface before and after thermal annealing under H_2 gas environment. a) Grain enlargement after thermal annealing. b) Removal of native oxide from the Cu surface. c) Surface normalization by smoothing high asperities.

As the growth of h-BN crystals on the Cu surface emerges from a nucleation site such as grain boundaries, the density of nucleation sites dictates the crystal placement and distribution, while surface defects limit the lateral spread of nano-material [4]. The previous reported results on Cu surface pretreatment [47] have not shown improvements (through a quantifiable metric relating surface pretreatment with crystal size or density). Thermal annealing alone cannot be used for surface preparation because of step edges and contaminant diffusion despite Cu grain enlargement and native oxide removal. Therefore, a subsequent processing step, such

as electropolishing, in addition to thermal annealing is required.

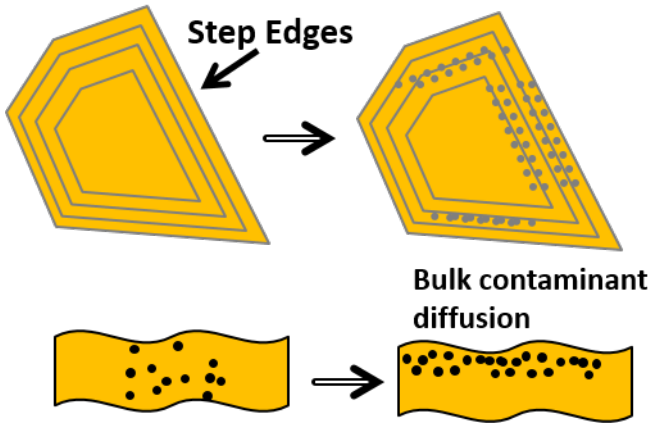

Figure 1.4: Impact of thermal annealing on Cu. a) Step edges become prominent. b) Contaminants from the bulk diffuse on to the surface. The diffusion direction is indicated by arrows.

This subsequent processing step is necessary to mitigate the effects of thermal annealing and to prepare a Cu surface for promoting high quality growth of h-BN. Electropolishing has been used as a surface preparation technique to flatten Cu foils to grow h-BN [4] and graphene [1, 2], however no quantifiable relationship such as roughness of Cu substrate with crystal size was established. Therefore, the aim of the work is to utilize thermal annealing and electropolishing of Cu to prepare a planarized copper substrate (or catalyst) by enlarging the Cu grains, reducing the density of nucleation sites, and surface defects, and enabling controlled growth of hexagonal boron nitride (h-BN). As electropolishing is a technique in electrochemistry, a brief discussion of electrochemistry followed by electropolishing is pertinent.

CHAPTER 2

Electropolishing: Theory and Practice

This chapter will introduce electrochemistry and also cover the theory and practice of electropolishing. The progression of different methods employed for this thesis will also be shown. Finally, the experimental procedure and the characterization techniques used will be discussed.

2.1 Electrochemistry

Electrochemistry is a branch of chemistry that studies chemical reactions at the interface of an electrode when the electrode is in an electrolyte solution. The basis of electrochemical studies lies in the electrochemical cell (shown in Figure 2.1), which has three basic components: a working electrode, where the reaction of interest is occurring, a counter electrode and an electrolyte (ionic conductor). When the electrical circuit is closed, with the application of a voltage potential to the electrodes in the electrochemical cell, chemical reactions involving oxidation and

reduction reactions take place between the electrode and the solution. The reactions in the cell can be divided into two half-cell reactions: anodic and cathodic reactions. The anodic reactions are all oxidation reactions, which lose electrons; while the cathodic reactions are all reduction reactions, which gain electrons. With these two simple half-cell reactions described, the study of electrochemistry has led to various applications such as batteries, electrolysis, corrosion, electroplating, of which electropolishing is one of the applications [58, 59].

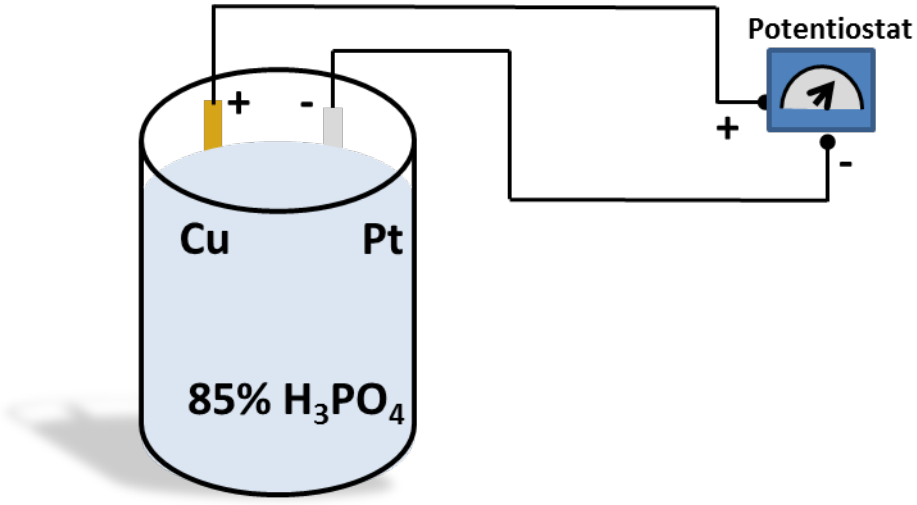

Figure 2.1: A simple electrochemical cell. The two electrodes: counter (Pt) and working electrode (Cu) is shown along with the electrolyte.

2.2 The theory and practice of electropolishing

Electropolishing is a technique where the working electrode (often metal) is etched away or dissolved in a controlled manner. The control is achieved both by choosing the appropriate electrolyte, that takes part in the dissolution process by accepting

metal ions (Me^{+}), and the appropriate applied potential on the working electrode that promotes the electrochemical reaction. Electropolishing has been used to prepare smoother and brighter metallic surfaces after mechanical preparation such as mechanical polishing, using fine abrasives such as diamond nanoparticles on a polishing pad, is inadequate. Both mechanical preparation and the usage of polishing pads will leave the metallic surface with various morphological complexities with both macroscopic (> 1 μm) and microscopic (< 1 μm) deformities. On a macroscopic scale the contour of a metal surface is filled with hills and valleys, and microscopic smaller hills and valleys exist on top of the macroscopic hills and valleys (discussed in detail in chapter 3). In this regard, electropolishing is used as a surface leveling process, evening the hills through controlled dissolution [12].

Upon application of an appropriate potential on the working electrode, the higher features (hills) are removed first and more quickly than the low regions (valleys) due to the existence of a concentration gradient and lower electrical resistance. Continued and prolonged potential application further reduces the high regions and leveling occurs at the microscopic level thus producing a planar surface without the presence of asperities. One of the first developments in metal electropolishing was published by Jacquet [60], investigating the electropolishing of copper in phosphoric acid by studying I-V characteristics. Unlike commonly expected, the I-V behavior of an electrochemical cell is non-linear (see Figure 2.2), with three discrete regions in the I-V profile, namely: etching, polishing or dissolution and gas evolution, with increasing applied potential [60, 61].

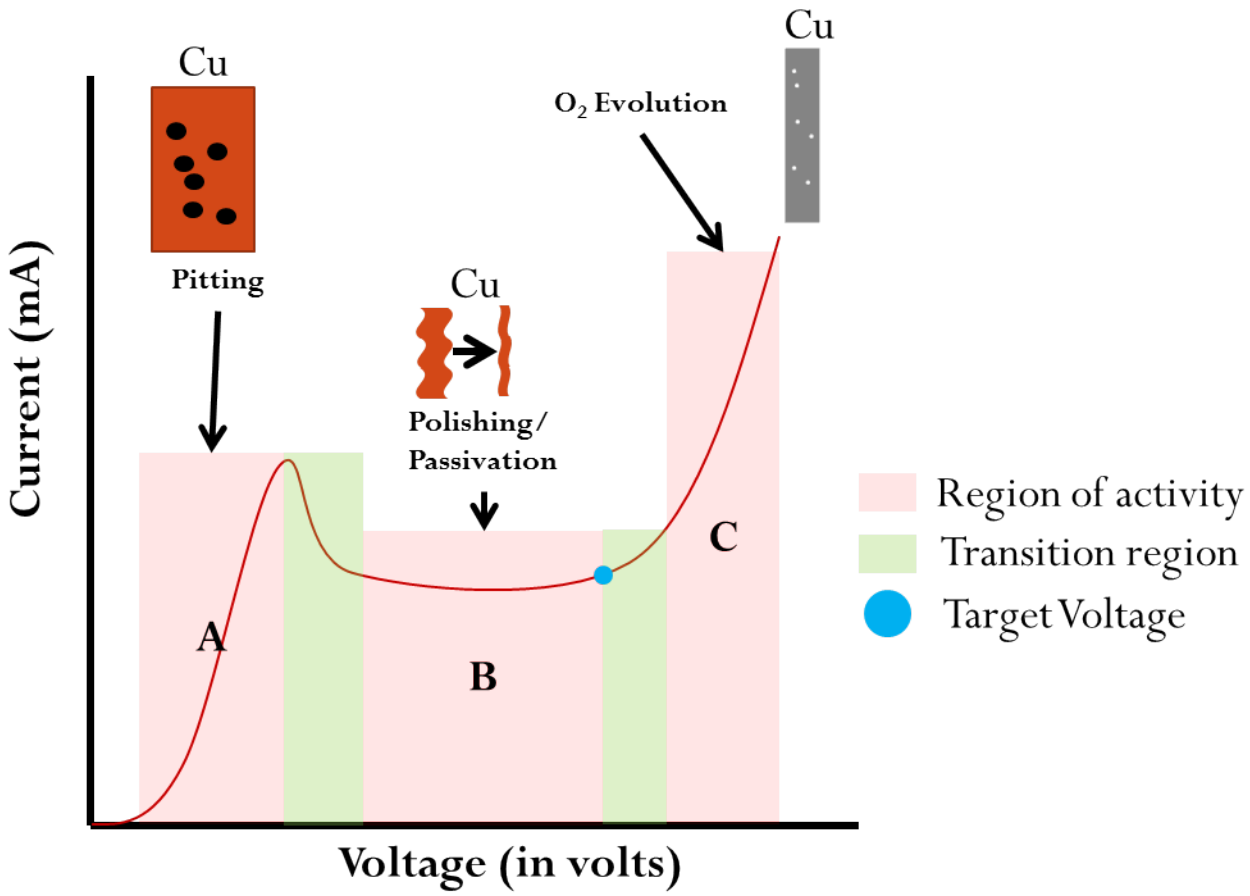

Figure 2.2: Current-Voltage relationship in an electrochemical cell for Cu electropolishing. The three regions: etching, dissolution and oxygen evolution is marked as A, B and C in the figure. Figure redrawn from [60]. The target voltage, also called inflection voltage due to transition from dissolution to oxygen evolution region, is indicated with a blue dot.

Each of these three distinct regions: Region A, B and C (as seen in Figure 2.2) have very distinct surface morphological activities occurring. It is however important to note that despite the characteristic model, under practice the curve (current-voltage) may vary (shifting or scaling) but nevertheless the form of the curves with

these three distinctive regions remain the same. Region A is where the Cu specimen is etched and a uniform removal of anodic material occurs throughout the Cu surface [60]. The transition region from A to B is characteristic of the onset of a viscous layer, which is formed on the anode surface that is responsible for polishing activity. Region B is the polishing/dissolution region, where polishing occurs and the current density (also called limiting current) drops significantly leading to a more selective removal of higher elements (hills). It is reported that the potential slightly less than the potential transiting from region B to C (indicated by a blue dot on the curve, target voltage in Figure 2.2) is where optimum electropolishing occurs [60]. Region C is where gas evolution (specifically O_2 evolution) occurs along with pitting which is ascribed to the formation of bubbles at random nucleation sites on the specimen surface [60]. Of these three regions, region B is the most relevant to this work as it is the region where the specimen surface undergoes electropolishing necessitating a closer examination. The viscous layer, which forms as the applied potential transitions from region A to B, is responsible for polishing.

As observed from the I-V profile, the viscous concentration layer (shown in Figure 2.3), which forms in the transiting region of A and B plays two roles. Primarily, the layer serves to introduce a back electromotive force (e.m.f) in the cell [60, 61]. And secondly, after the back e.m.f is attained, it serves to limit the current through the cell. Elmore finds that the concentration layer is produced by slow diffusion of freshly dissolved anode material into the bulk of the electrolyte [61]. It is understood that the current through the cell is carried by highly mobile hydrogen ions and is responsible for the removal of the anode material by diffusion [61]. The con-

centration of the dissolved copper in the concentrated layer is set by an upper limit of solubility of copper in the phosphoric acid electrolyte. When the concentration layer has grown to an extent that this upper limit is reached, the current density will be automatically limited by the rate of diffusion of dissolved copper away from the anode. This situation is responsible for the lowering of current in the A-B transition region [61, 62].

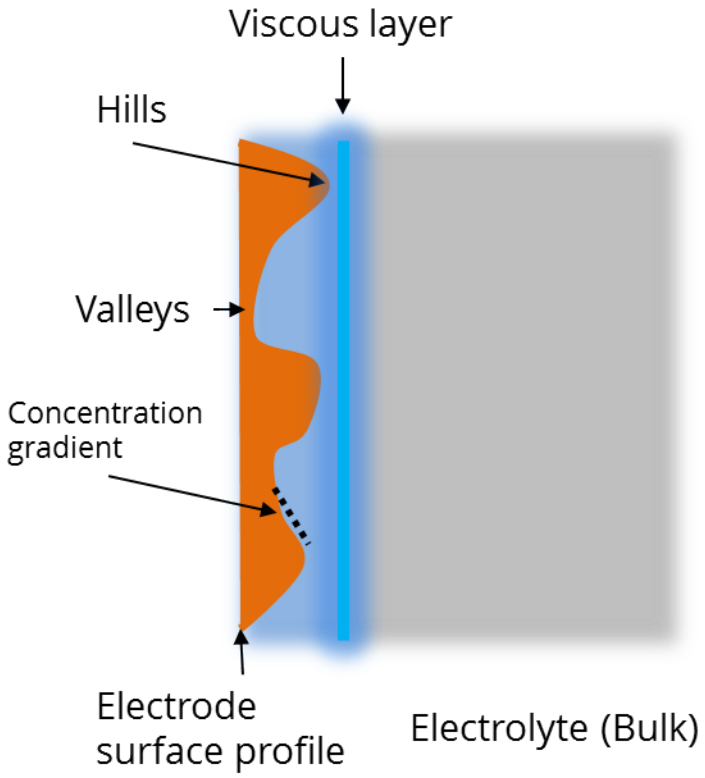

Figure 2.3: Formation of viscous layer at the electrode and the concentration gradient at the surface asperities.

The polishing effect, which takes place in region B, occurs when the rate of solution of copper is limited by the concentration gradient at the anode as shown in Figure 2.3 [61, 62]. As the gradient is the greatest near the projecting por-

tions of the surface, these portions dissolve more rapidly than the other regions of the surface [61, 62]. To account for polishing on the basis of diffusion, the following assumptions are made. For a plane anode, the current can be given by $i = -AFD(\partial c/\partial x)_{(x=0)}$, where F is the faraday, c is the concentration of the metal, A is the area of the electrode and D is the coefficient of diffusion of dissolved metal [62]. When the current is passed for a certain time, t_0, the concentration at the anode surface reaches a maximum value, c_m, represented by the solubility limit of the metal in the electrolyte. At times much greater than t_0, the current is limited by the concentration gradient at the anode which is valid when no new anode reaction, such as salt precipitation, takes place. From these assumptions, metal will diffuse from high points on the surface much more rapidly due to steep concentration gradients than from depressions on the surface. As the high regions are removed, the anode surface will become progressively smoother leading to electropolishing [61,62].

2.3 Progression of methods for this work

2.3.1 Method A

The initial work for this project was to replicate the setup and results from the Cu electropolishing literature [60, 61, 62], which will be denoted as Method A. The electropolishing setup (now referred to as standard electropolishing technique) in the literature has four components: power supply unit, electrolyte (85% concentrated H_3PO_4), Cu working electrode and Pt counter electrode [60, 61, 62]. As shown in

Figure 2.4, I prepared the setup for method A using an Agilent E3640 DC power supply to apply a potential on the electrodes, 85% concentrated phosphoric acid as electrolyte, Cu as the anode, and Pt as the cathode. The Cu cathode is a $\approx$ 20 mm $\times$ 10 mm foil (27 µm thickness, Sigma Aldrich) and the Pt cathode is $\approx$ 40 mm $\times$ 15 mm foil (200 µm, Sigma Aldrich). In order to determine the front (facing the cathode) and the back of the Cu anode, I cut a triangular piece on the lower left side of the Cu anode which will face the Pt cathode (shown in Figure 2.5). Prior to electropolishing, I blew nitrogen across the electrodes to remove any dust or debris. An insulating tape was used to hold the electrodes on an aluminum strip and the aluminum strip is suspended from a Teflon block ceiling acting as a clamp (shown in Figure 2.5) which is placed on top of the glass beaker. The electrolyte is poured into an 80 mL beaker after checking for electrical continuity of connections between the electrodes and the power supply. The Cu anode is $\approx$ 80% submerged into the electrolyte (shown in Figure 2.5), such that a portion of the anode that is not in contact with the electrolyte can be used for visual comparison of the apparent surface finish with the region that undergoes electropolishing. I took care to make sure that the electrolyte does not come in contact with the aluminum strip and the insulating tape that is holding the anode so that electropolishing is confined to the Cu anode. I finally applied a potential of $\approx$ 1.5 V, as commonly reported in the literature, on the Cu anode for pre-determined time periods: 5, 10, 15, and 30 minutes.

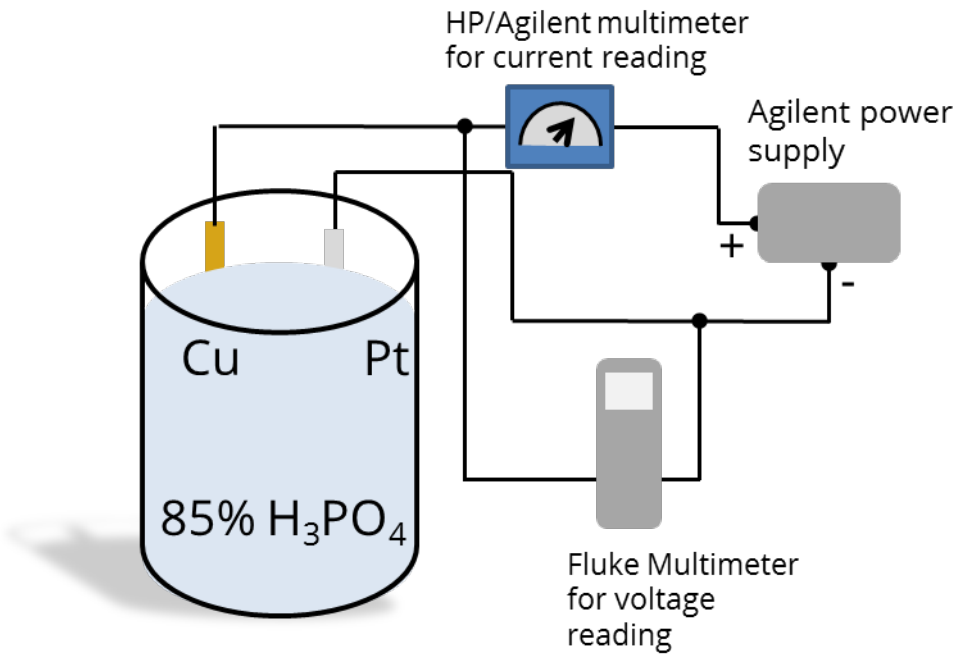

Figure 2.4: Electropolishing setup for Method A. Power supply: Agilent E3640 DC power supply, HP/Agilent 34405A multimeter as ammeter, and Fluke 170 series multimeter as voltmeter.

Before the application of a potential to the electrolytic cell, I logged the voltage reading from the voltammeter (Fluke 170 series multimeter) after the electrolytic cell is setup. When the potential was applied, using the voltage reading of the applied potential was recorded. The power supply does not log current and voltage, therefore the current-voltage (voltammetric) and current-time (chronoamperometric or limiting current) relationship cannot be determined. However, I logged the initial and final current using an HP/Agilent 34405A multimeter, where initial current was noted when a potential is applied to the cell at the beginning of the pre-determined time period and the final is noted at the end of the pre-determined time period,

immediately prior to when the applied potential is switched off. The initial current values were much higher than the final current despite the power supply holding a constant applied potential throughout the electropolishing duration.

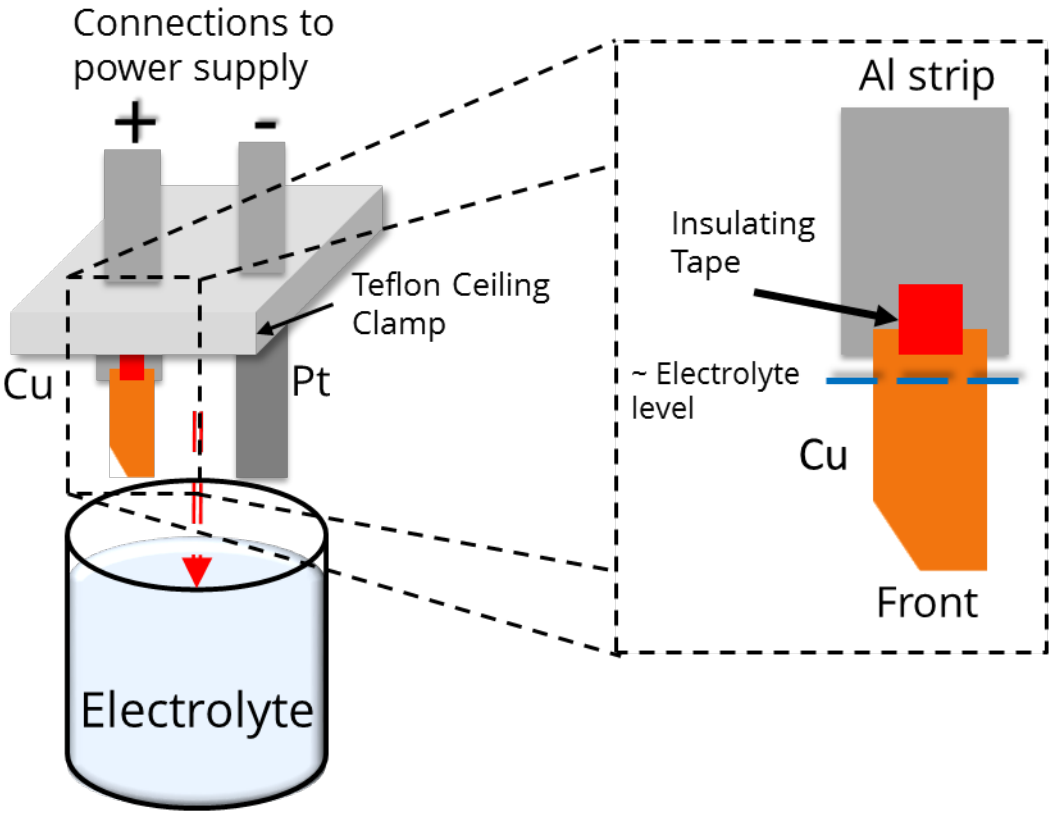

Figure 2.5: Experimental setup of the electrolytic cell for Method A.

After the electropolishing was performed, I removed the Cu anode first and rinsed thoroughly, followed by the Pt cathode. The rinsing was done by running DI water over the electrode surface. However, when I observed the Cu surface it was often unclear if polishing actually took place as there was no difference between the surface finish of the anode that is submerged into the electrolyte and the portion that was not in contact with the electrolyte. Upon further inspection using the op-

tical microscope and Nomarski-contrast[1] images, there was still no visible difference between an electropolished Cu surface and the vendor supplied Cu surface, which was used as the control sample. It was unclear if the setup was faulty or the applied potential had no effect on the electropolishing. Therefore, this method was decided as ineffective for a variety of reasons. There was no consistent electropolishing occurring from sample to sample as the grooves on the Cu surface remained intact. There was also no information about current as a function of time and if the cathode had any role in retarding the conductivity in the circuit.

2.3.2 Method B

A new setup, Method B (shown in Figure 2.6), was created replacing the power supply with a Gamry Interface 1000 potentiostat. A potentiostat is an instrument used to control the electrode potentials, and log the potential and current during the electrochemical process. The electrolytic cell remained unchanged with Cu anode and Pt cathode, and concentrated H_3PO_4 electrolyte. The electrodes are clipped against beaker walls using alligator clips instead of a Teflon clamp. The alligator clips are used because the Teflon clamp is susceptible to movement and could topple the beaker with the electrolyte while loading and unloading of samples and connections. Connections are once again checked before pouring the electrolyte in the beaker, where the Cu anode is $\approx 80\%$ submerged into the electrolyte (as shown in

[1]Nomarski or Differential Interference Contrast (DIC) images are obtained from the transformation of the phase shift of light into detectable amplitude differences from the optical path differences within the specimen

Figure 2.5). Before performing electropolishing, I studied the voltammetric behavior to find the target potential, which is the inflection potential at the intersection of the plateau region and pitting region. The current levels as high as 80 mA were observed while performing voltammetry. The applied potential, which varied from sample to sample, was chosen to be as 90% of the inflection potential as it is slightly less than the gas evolution potential as suggested by [61]. The average applied potential is $\approx$ 2.05 V with a variance of 0.044 V and the inflection potential is $\approx$ 2.26 V with a variance of 0.0577 V. Electropolishing is done using chronoamperometry for the calculated applied potential and a pre-determined time period: 15, 30 and 45 minutes. After the electropolishing is performed, the electrodes are rinsed with running DI water on the electrodes.

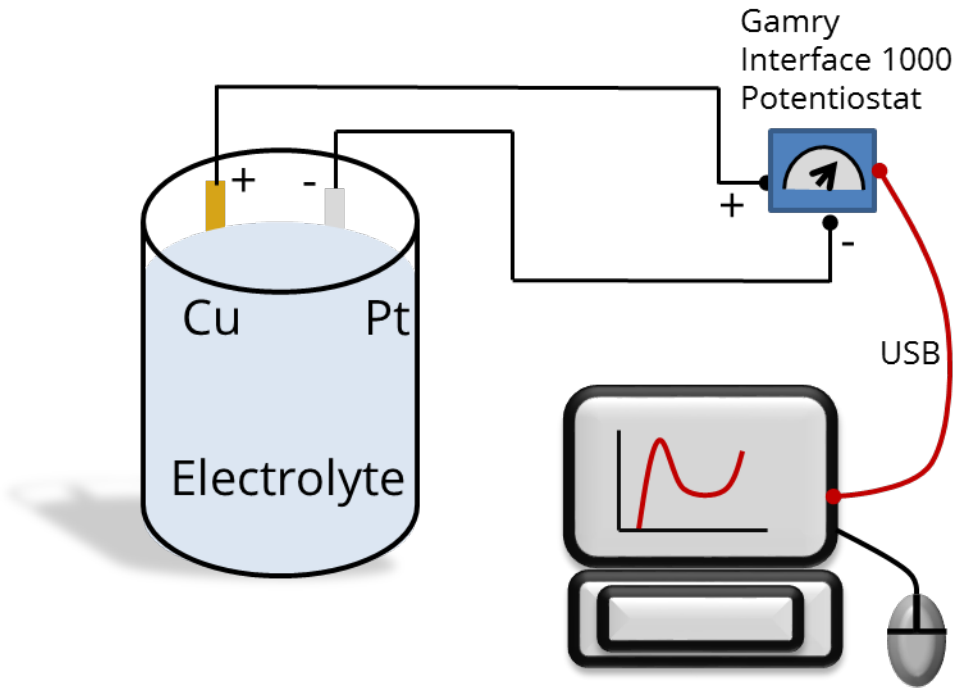

Figure 2.6: Experimental setup of the electrolytic cell for Method B.

The initial electropolishing results were inconsistent but there were samples where electropolishing occurred clearly by visual inspection. It is understood that if the connections from the cell to the potentiostat were not right, it will result in spikes in voltammetry. As all the components of the setup were "fresh": Cu anode and electrolyte, I became suspicious of the Pt cathode, as its reuse may be the cause of inconsistent voltammetric results. Therefore, the used platinum cathode is replaced with a fresh Pt anode and electropolishing is performed. I observed that the electropolishing occurred successfully for two sequential runs but the following runs became inconsistent, thus confirming that the used Pt cathode was responsible for inconsistent results. The cathode was dipped in nitric acid to remove any copper salts prior to electropolishing. After using the cathode cleaned with nitric acid, voltammetry was performed to inspect the magnitudes of current, which is proportional to the electropolishing rate. If electropolishing is indeed happening, the currents can reach as high as 80 mA. However, this was not observed.

Upon conducting a literature review for platinum cathodes in electrochemistry, [63] reported that a 600-A sanding paper is used to scrub the Pt electrode after electrochemical experimentation. Using the same sanding paper, the Pt electrode was scrubbed on both sides of the electrode and blown with N_2 gas. I performed repeated voltammetry tests to check the reusability of the Pt cathode by assessing the current magnitude after the scrubbing process. Chronoamperometry is also performed after the cathode shows reusability. Chronoamperometry shows a $y = 1/x$-like profile i.e. the current decreases following this profile with increasing time. After the electropolishing is performed, the electrodes were rinsed with running DI

water on the electrode, acetone rinse and DI water rinse. I adopted the acetone rinse as the DI water does not always rinse away the electrolyte residue from the Cu surface.

I observed that the electropolishing was occurring consistently as there was visible brightening of the Cu sample relative to a dull finish observed on vendor supplied Cu sample. At this point, I understood that for electropolishing to occur, a potentiostat and a clean Pt cathode is necessary. The electropolishing results were confirmed after examination under the microscope using both optical and Nomarski images. The Cu surface morphology changes with increasing electropolishing time: 10, 15, 30 and 45 minutes, where the irregularities on the Cu received from the vendor become more leveled after electropolishing. The Cu foil becomes much thinner losing as much as a third of its thickness (from $\approx$ 27 μm to about $\approx$ 18 μm). Due to significant thinning, electropolishing performed beyond 30 minutes has been inconsistent as the sample is torn along the region 80% submersion line (as shown in Figure 2.7). I observed an increase in current magnitudes when the electrolyte is reused. Therefore, a fresh electrolyte (concentrated H_3PO_4) has always been used so the Cu samples after electropolishing can be compared sample to sample (discussed in detail in chapter 3). There was also some visible contamination occurring despite the cleaning process of DI water rinse, acetone rinse and DI water rinse. Despite electropolishing the surface, etch pits were observed on electropolished samples. Therefore, it was necessary to reduce the applied potential to 1.8 V ($\approx$ center of the dissolution region) as it was too close to the gas evolution regime where pitting occurs.

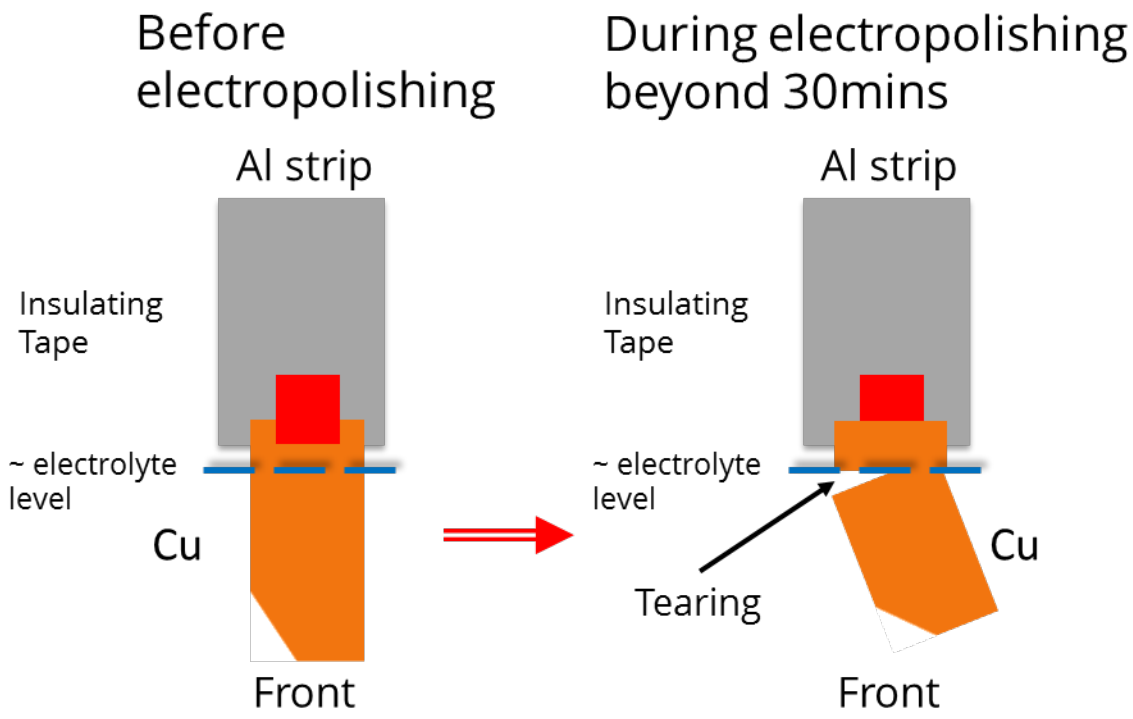

Figure 2.7: Tearing of the Cu sample during the electropolishing process beyond 30 minutes. The point where the Cu sample is torn due to significant thinning is indicated with the arrow.

Etch pits (as shown in Figure 2.8) are reported to occur inherently with polishing in concentrated H_3PO_4 [64, 65, 66, 67, 68]. Etch pits are ascribed to oxygen bubbling at random nucleation sites on the Cu surface causing a spherical dent (> 50 µm in diameter and $\approx 2 - 4$ µm deep) on the surface. It is clear that the etch pits will disrupt the surface morphological continuity and there is no visible electropolishing occurring at the site of the etch pit i.e. the surface morphology with the irregularities stay intact. There were several reports in the literature for using additives to prevent oxygen bubbling by using organic acids such as acetic acid. Organic

acids such as acetic acid along with organic alcohols such as methanol, polyethylene glycol, ethylene glycol, were reported to promote planarization efficiency of Cu surface and a two-additive, combination of organic acid and alcohol, were reported to show greater planarization efficiency [65, 66, 67, 69, 70]. The role of the organic acid is to increase the acidity of the electrolyte and thus the electropolishing rate. While the role of organic alcohol is to inhibit the dissolution rate and increase the viscosity of the electrolyte [65, 66, 67, 69, 70]. The two-additives also undergo esterification reaction which is shown to promote planarization [65, 66, 67, 69, 70]. It is also reported in the literature that organic acids also limit oxygen bubbling at the Cu surface increasing the viscosity of the compound electrolyte and the alcohol promotes wetting of the Cu surface [66].

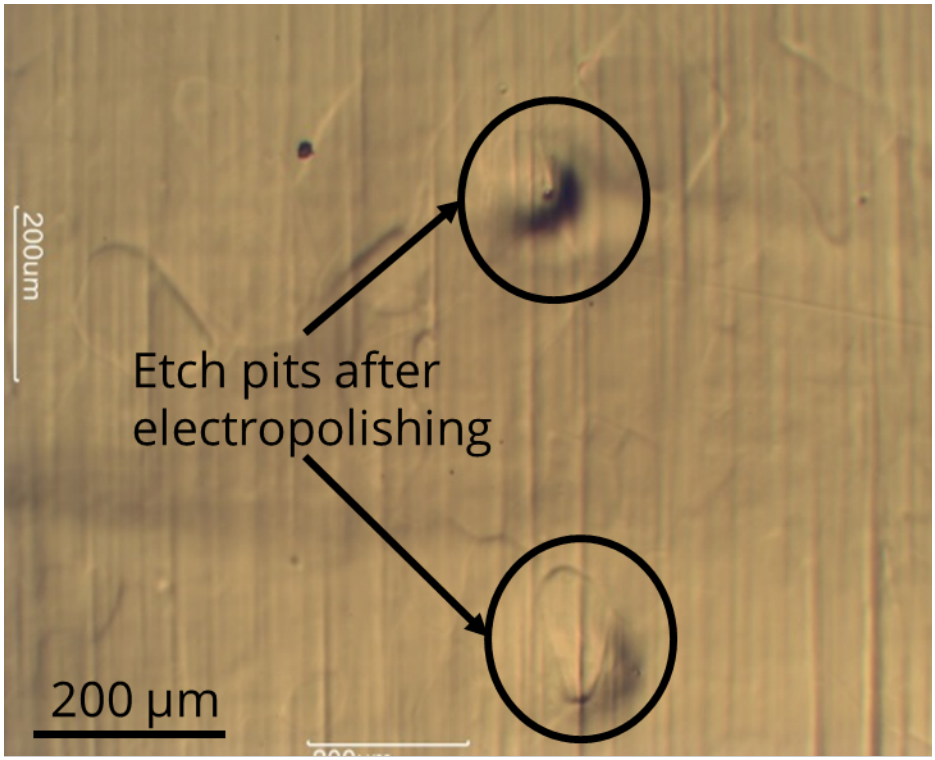

Figure 2.8: An example of etch pits (large ones) that occur with standard (concentrated H_3PO_4) electropolishing. The diameter of the etch pits are ≈ 100 µm.

For the initial experimental additive tests, methanol only is used as an additive (25% electrolyte concentration by volume). Because of inconsistent results, methanol is discarded as an additive for my electropolishing experiment. Similarly, concentrated acetic acid (25% concentration by volume in the electrolyte) is used along with concentrated H_3PO_4 for electropolishing for 15 minutes at 1.8 V. The results are much more promising with electropolishing occurring throughout the Cu anode and fewer etch pits being observed. Acetic acid has been reported to show positive results as an additive for Cu electropolishing [70]. Ethylene glycol, which was also reported in the literature as an alcohol additive and Cu dissolution inhibitor

for electropolishing, has been chosen [69].

The following electrolyte mixture was prepared by volume: 25% glacial acetic acid, 25% ethylene glycol and 50% concentrated H_3PO_4 (20 ml, 20 ml, 40 ml, respectively), was prepared in a 100 ml beaker. The concentration choice was guided by the literature [66, 70]. After setting up the electrodes and the connections as in method B, the electrolyte solution was thoroughly stirred and poured into a 40 ml beaker. A cleaning procedure was also developed for rinsing electrolyte after electropolishing by replacing acetone with methanol, as rinsing with methanol was observed during earlier trials to have a qualitatively brighter Cu surface than acetone rinse.

Electropolishing tests by using cyclic voltammetry was performed to assess the viability of using additives for electropolishing; the results are discussed in detail in chapter 3. Chronoamperometry is performed at 2.3 V (center of the plateau region, see Figure 2.2) potential to see the limiting current behavior of the electrolytic cell. I noticed that electropolishing took place, along with significant reduction in etch pits observed using optical and Nomarski images. Thus, I chose this compound two-additive electrolyte to be part of a new electropolishing recipe for CVD growth studies.

2.3.3 Method C

A new method, Method C, was developed from the consistency, reproducibility and evolution of results from the previous method, Method B and to be used for growth

of h-BN on electropolished Cu. A Gamry Reference 3000 potentiostat and the electrochemical cell setup that is identical to method B was utilized. The applied potential was reduced to 1.8 V for concentrated electrolyte to reduce any potential etch pits from forming at the Cu anode and 2.3 V for two-additive electrolyte. These voltages are approximately in the center of the dissolution region, away from the gas evolution potential. The electropolishing time is now limited to 30 minutes to ensure the Cu samples' structural integrity. Pt cathode is scrubbed with a 600-A sanding paper prior to electropolishing. Both the Cu and Pt electrodes are cleaned with N_2 gas. Electropolishing is performed for 30 minutes and the Cu samples are rinsed off with running DI water on the electrode surface followed by methanol rinse and finally running DI water on the electrode surface.

2.3.4 Experimental Plan

An experimental Cu sample preparation plan for growth was now designed using both vendor supplied Cu (Cu) and thermally annealed Cu (Cu TA) at 1030°C in H_2-N_2 atmosphere for 5 hours. Electropolishing was done on both Cu and Cu TA using a concentrated electrolyte and two-additive electrolyte electropolished at 1.8 V and 2.3 V, respectively for 30 minutes. Figure 2.9, shows the general flowchart of the experimental plan. Electropolishing is performed as described in Method C. AFM and SEM of both Cu and Cu TA sample is taken. Electropolishing is performed for 30 minutes for both Cu and Cu TA in concentrated H_3PO_4 and using the 2-additive process at 1.8 V and 2.3 V respectively.

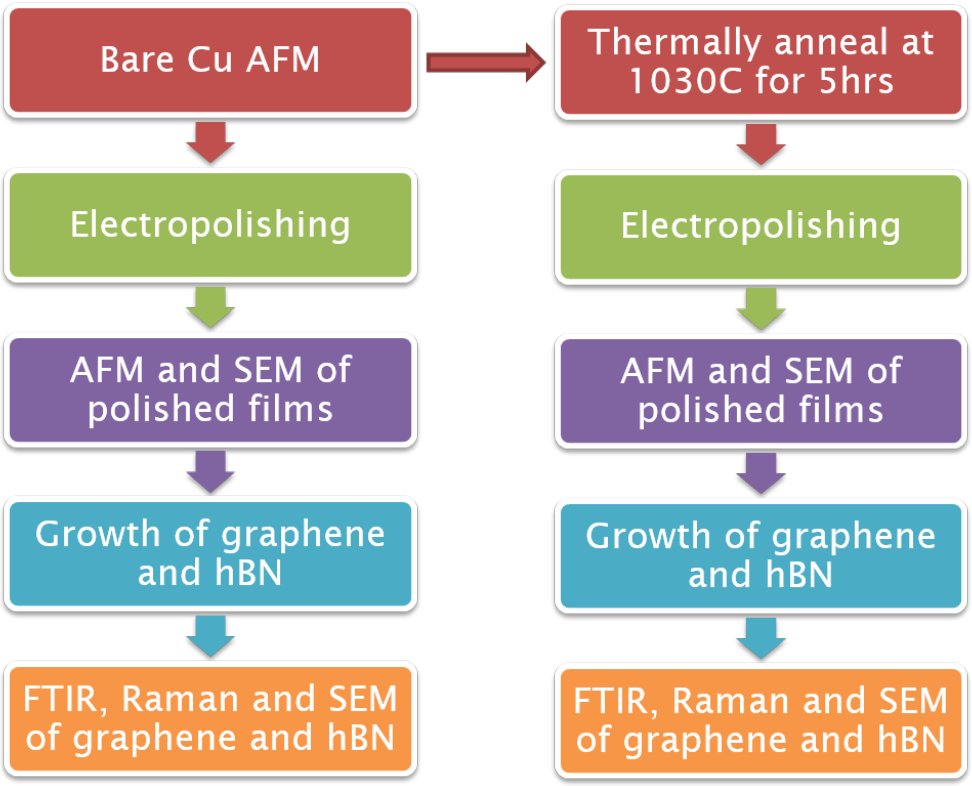

Figure 2.9: Cyclic voltammetry and chronoamperometry (limiting current) of electropolishing performed in concentrated (85% concentrated) H_3PO_4 in a and b, respectively. The increase in current observed from reusing the electrolyte is indicated in a and b.

The results are discussed in chapter 3 starting with electropolishing results from method B. The surface morphological state of Cu (Cu and Cu TA) from optical images and AFM is discussed. The comparative results of Cu surface evolution through electropolishing in concentrated and 2-additive process is discussed to show surface morphology changes along with the roughness evolution on Cu TA is also shown.

2.4 Characterization Techniques

There are three characterization techniques utilized for this work: Scanning electron microscope (SEM), Attenuated Total Reflectance Fourier Transform Infrared Spectroscopy (ATR-FTIR), and Tapping Mode Atomic Force Microscopy (TM-AFM) with phase imaging mode.

SEM is a type of electron microscope that produces images of a sample by rastering it with a focused beam of electrons. Modern SEMs provide a resolution ranging from 1 nm to 10 nm, therefore making it much more superior than optical light microscopes. SEMs generally have a large depth of focus i.e. if the specimen features are away from the focal plane, they appear almost sharply in-focus [71].

ATR-FTIR is a form of infrared spectroscopy whereby the infrared beam is directed onto the sample at a critical angle resulting in total internal reflectance. The internal reflection creates an evanescent wave close to the sample surface. The evanescent wave is attenutated after interacting with the sample. The attenuated wave is reflected back into the detector in the spectrometer resulting in an infrared spectrum [72].

Atomic Force Microscopy (AFM) is a high-resolution scanning probe microscopy (SPM) technique used to probe the morphology of sample surface without damaging the sample surface. In tapping mode AFM, a cantilever beam ($\approx$ 150 μm) with a sharp tip ($\approx$ 20 nm tip radius) is oscillated (amplitude $\approx$ 50 nm) at its resonant frequency ($\approx 100 - 300$ kHz) and scanned across the sample surface (around 20 μm

$\times$ 20 μm size). As the cantilever tip gets close to the surface, there is an interaction of forces with the surface. The interactive forces between the tip and the sample causes the amplitude to decreases as the tip gets close to the sample; a phase signal is also obtained from the difference in amplitude oscillation. A piezoelectric actuator is used to adjust the height (tip-sample distance). A tapping mode AFM image is produced by imaging the interactive forces between the tip and the sample. The resolution of AFM is limited by the tip radius of the cantilever beam and in general gives a resolution of 10-20 nm [73].

CHAPTER 3

Results and discussion of Cu electropolishing and surface evolution

This chapter will cover the outcome of copper electropolishing results and the morphology of copper surface after electropolishing. It will also discuss Cu electropolishing performed using a potentiostat using voltammetry. This will be succeeded by a discussion on the surface morphology of copper as received from the vendor (Cu) and after thermal annealing (Cu TA) using optical microscopy and atomic force microscopy (AFM). To overcome the side effects of the standard electropolishing recipe using only concentrated H_3PO_4 electrolyte, electropolishing using the two-additive electrolyte is used and the results is discussed in detail. Finally, roughness measurements of the Cu surface after each processing step and the morphology of Cu surface after electropolishing using the two-additive electropolishing using AFM and SEM will be discussed.

3.1 Electropolishing of Cu anode

A non-linear I-V profile is observed for Cu electropolishing with three distinct regions: etching, plateau (dissolution) and pitting or gas evolution region. The voltammetry profile, shown in Figure 3.1a, is obtained using method B utilizing a potentiostat. The applied potential is selected to be 90% of the target potential because it is approximately the potential for optimum electropolishing [60] and also avoids oxygen evolution [60, 62] from occurring. The results of the voltammetric (I-V) and limiting current behavior of the as received Cu anode is shown in Figure 3.1b. The voltammetry shows the expected three distinct regions with the inflection potential (gas evolution potential) and the applied potential (90% of the gas evolution potential) clearly indicated. The limiting current for the calculated applied potentials (shown in the legend for Figure 3.1) follows an exponential profile, indicating formation of a resistive viscous concentration layer [61, 62] through the dissolution of Cu from the surface immediately after the application of voltage.

Using a fresh electrolyte a very similar I-V and limiting current behavior between runs was observed, indicating reproducibility. However, when the electrolyte from the previous electropolishing run was reused, there was an increase in current as indicated in voltammetry and limiting current plots in Figure 3.1. This can be ascribed to the accumulation of Cu^{2+} ions in the reused electrolyte. Thus, it is important to use a fresh electrolyte as the electropolishing rates will be similar and reusing the electrolyte may lead to incomparable electropolishing results.

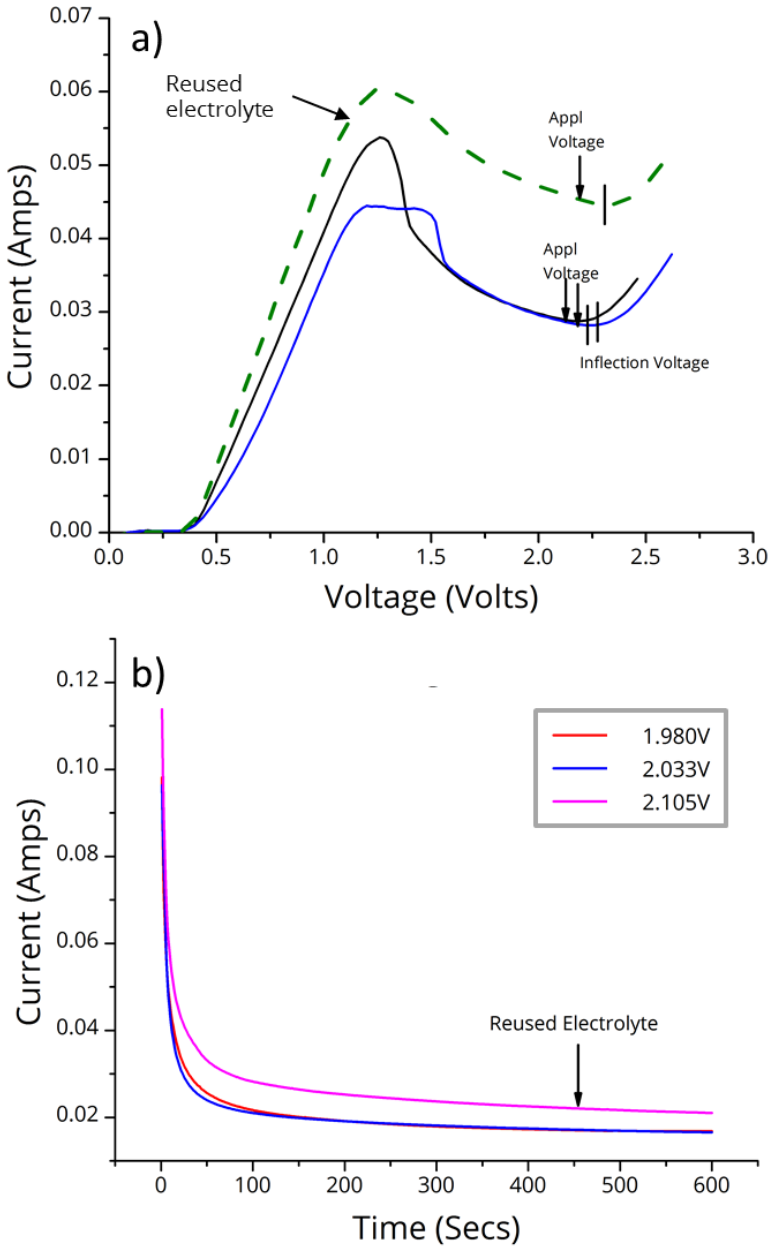

Figure 3.1: Cyclic voltammetry and chronoamperometry (limiting current) of electropolishing performed in concentrated H_3PO_4 in a and b, respectively. The increase in current observed from reusing the electrolyte is indicated in a and b.

3.2 Surface morphology of Cu: Before and after thermal annealing

The polycrystalline copper foils, as received from the vendor (henceforth referred to as Cu), is expected to be very rough with the presence of massive irregularities arising from the metallurgical rolling process (as discussed in section 1.3 shown in Figure 1.2). The features are large enough to be observed from optical and Nomarski images (see Figure 3.2). Thermally annealed Cu (Cu TA) is prepared from Cu by treating foils in a flowing H_2-N_2 atmosphere at 1030°C for 5 hours. After thermal annealing, the Cu TA is smoother in profile than Cu before annealing (see Figure 3.2 d and a) while also enlarging the grains. The enlarged grains are expected to be hundreds of microns in size as seen optically in Figure 3.2d. Cu TA also shows the presence of rolling lines (see Figure 3.2). The rolling lines and the rolling directions are shown in Figure 3.2 a and d for Cu and Cu TA, respectively.

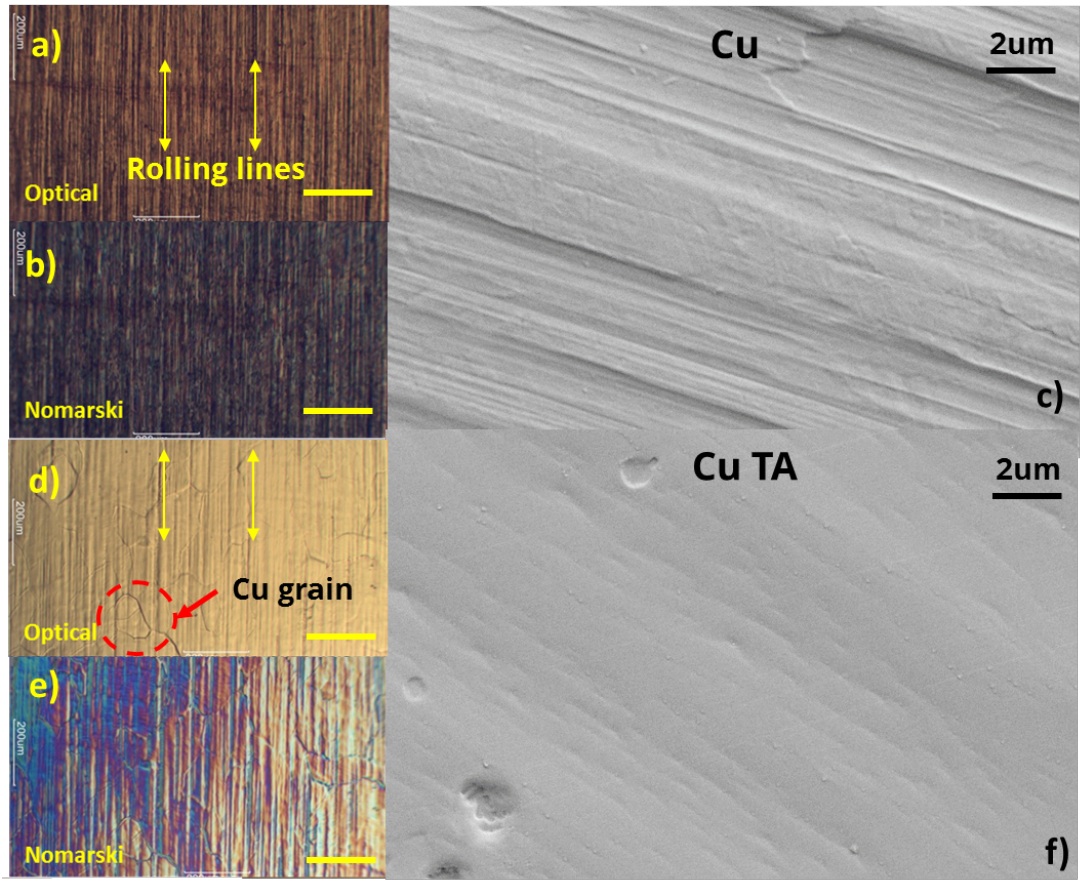

Figure 3.2: Optical (above) and Nomarski (below) images of Cu (a, b) and Cu TA (d, e) under the microscope (5x magnification). SEM images shown in c and f are a localized view of the Cu and Cu TA surfaces, respectively. The direction of rolling lines are indicated in Cu and Cu TA, a and d, respectively. The Cu grain, which enlarges and becomes more visible after thermal annealing, is indicated using the red dashed circle. The scale bar is 200 μm for optical images and 2 μm for SEM images.

Tapping mode atomic force microscopy (AFM) is performed to assess the surface morphology of Cu and Cu TA (Figure 3.3). From the AFM images, the

appearance of macroscopic irregularities on Cu is clear and the microscopic features are much more distinguishable. A deep sinusoidal-like profile (Figure 3.3) in the rolling lines is clearly evident in Cu. The macroscopic irregularities from rolling of Cu have a width > 4 μm and height ranges from 100 nm to 400 nm. Microscopic irregularities (< 1 μm in width) lie on top of the sinusoidal-like macroscopic profile. The AFM image of Cu TA shows lower variations in height than Cu and reveals step-like features.

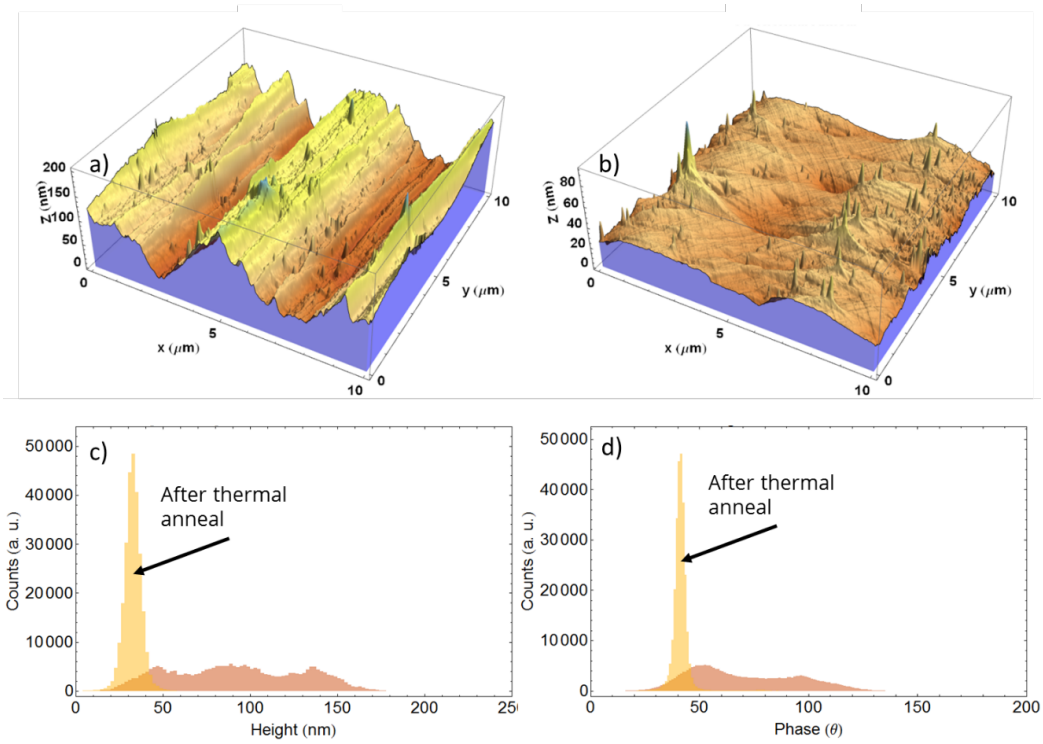

Figure 3.3: A 10 μm × 10 μm tapping mode atomic force microscopy profile of Cu before and after thermal annealing, a and b respectively. c and d show the histogram of height and phase distribution of Cu data before and after annealing (indicated).

A histogram of the height and phase data of Cu and Cu TA is obtained from the AFM images (see Figure 3.3 c and d). The rougher Cu shows multiple bell-

shaped distributions quantifying the distinct microscopic and macroscopic profiles of the non-uniform surface. The Cu TA shows a single bell-shaped profile in the height histogram indicating a uniform surface. The Full Width Half Maximum (FWHM) of the bell-shaped distribution of height for Cu TA is also narrower ($\approx$ 20 nm) than Cu ($\approx$ 100 nm). The grain enlargement in Cu TA by merging adjacent grains is responsible for creating a uniform surface which will be discussed. The phase image, a secondary imaging technique of tapping mode AFM arising from differences in tip-sample adhesion, is used to map the material variations on the surface. Therefore, if the Cu TA surface has a single crystallographic orientation throughout the scanned region (10 μm $\times$ 10 μm), the adhesion between the tip and the surface should be alike in the scanned region. As the AFM scan region is much smaller than the Cu TA grain size ($>$ 100 μm as noticeable in Figure 3.2), the AFM image of Cu TA is expected to have a single grain orientation and thus a single bell-shaped distribution in phase histogram as shown in Figure 3.3d. In contrast, Cu shows multiple bell-shaped peaks indicating the existence of various orientations within the AFM scan regions. Despite the uniformity shown by Cu TA, there are "spike-like" features that are visible on Cu TA but are harder to see on Cu as they are dominated by much larger features on the Cu surface.

Although the smoothing effect takes place on the whole Cu surface after thermal annealing, the spike-like features (shown in Figure 3.3b) are more prominent in Cu TA. The distribution of these spike-like features also seem very random. AFM height and phase image reveal that the spike-like features (or spot-like features in a 2D representation) can in fact be potential nucleation sites as indicated in Figure 3.4

a and b. AFM phase imaging, which reveals the difference in surface material composition from the phase contrast, also clearly shows the potential nucleation sites (indicated in Figure 3.4b) are in the same region as height images. The phase images also indicate that the nucleation sites appearing like spots can be materially different from Cu (such as Fe, Al). This conclusion is arrived from the fact that AFM on Cu TA was performed on a grain with a single orientation. Therefore, any differences in height should not be marked by difference in the phase contrast due to material uniformity. And any difference in orientation or material should have a direct effect on the phase signal. To confirm that these spots are not artifacts arising from the AFM imaging, SEM is performed on a similar Cu TA sample which reveal the existence of similarly sized spots (see Figure 3.4d), which are few hundred nanometers in diameter. A line scan is obtained from the AFM height image (as shown in Figure 3.4c) showing that the diameter of these spots are several hundreds of nanometers in size with a height of few tens of nanometers (see Figure 3.4c). Despite the smoothing occurring with thermal annealing, these nucleation sites (spots) may also act as surface abnormalities impeding lateral growth. Therefore, another surface processing step such as electropolishing becomes necessary not just for surface smoothing but also to reduce the nucleation sites.

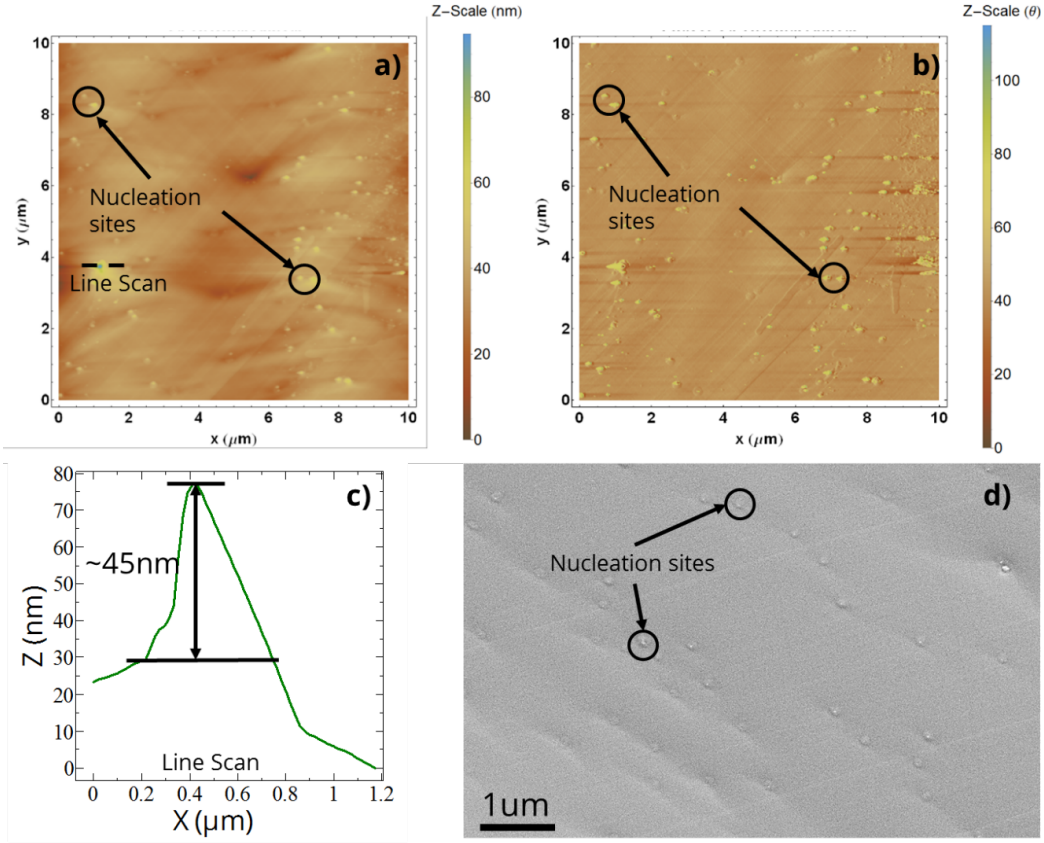

Figure 3.4: Tapping mode AFM of Cu TA surface with, a) height, and b) phase image. c) A line scan of a potential nucleation site is also shown as an example. d) SEM image of Cu TA. The potential nucleation sites are clearly visible and marked on both the AFM and SEM images.

3.3 Cu surface evolution after thermal anneal and electropolishing

The essence of this project is to modify the Cu surface after thermal annealing using electropolishing to create a smoother surface. The Nomarski and optical images, as shown in Figure 3.5, show the evolution of Cu surface from the as received state to

the thermally annealed state and with varying electropolishing duration of Cu TA (c thru e in Figure 3.5). A longer electropolishing period of Cu TA shows a much more uniform, planarized surface while the shorter period still retains the sinusoid-like profile observed both by optical and Nomarski images. Irrespective of the duration, the step edges of Cu TA, which are more clearly seen in the Nomarski, are removed within 15 minutes of electropolishing. However, longer electropolishing is needed to further smoothen the surface. It is observed that during electropolishing, etch pits form on the surface as shown in Figure 3.5f. As electropolishing dissolves Cu from the surface, any native oxide present on the surface prior to electropolishing should also be stripped off during this electropolishing process.

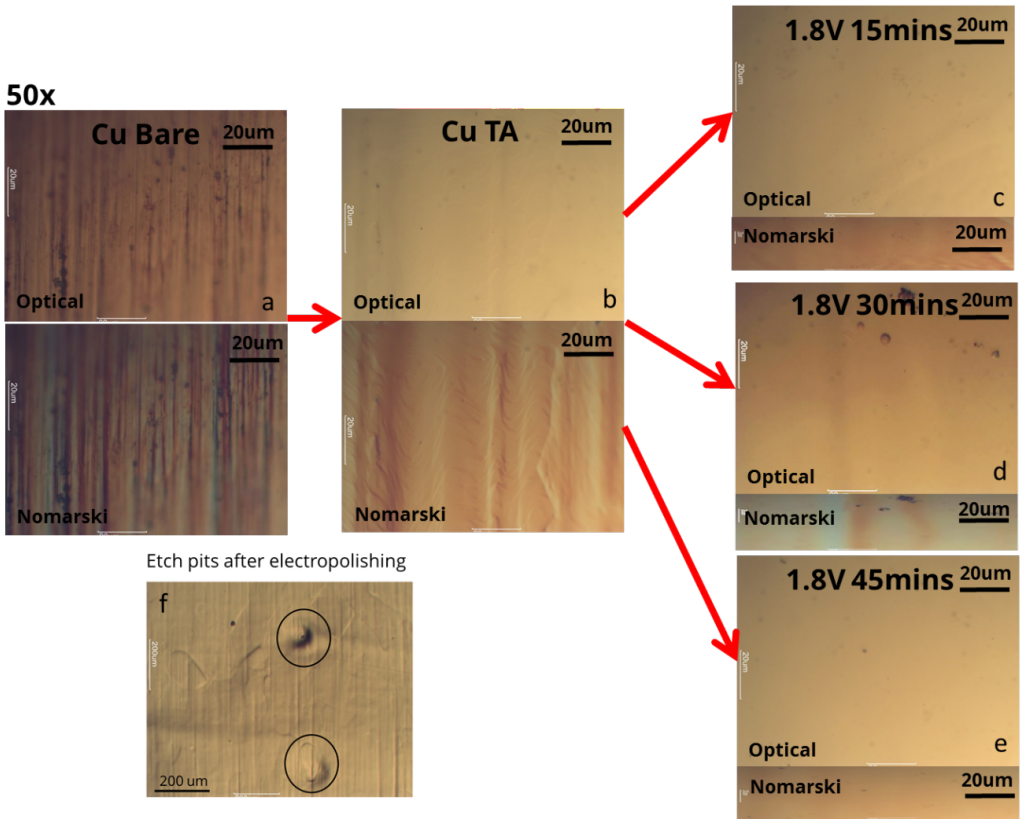

Figure 3.5: Optical and Nomarski images of surface morphology evolution of Cu before and after thermal annealing and evolution of Cu TA with the duration of electropolishing time: 15, 30 and 45 minutes (c, d and e, respectively). f) Example of etch pits forming on the Cu surface during electropolishing.

X-Ray Photoelectron Spectroscopy (XPS) is performed to quantify the presence of native oxide in two different valence states (Cu(II) and Cu(I)) on Cu before and after thermal annealing and after electropolishing. Figure 3.6 shows the high resolution spectrum of Cu 2p performed on Cu, Cu TA and Cu TA electropolished (Cu TA EP) for 1.8 V for 15 minutes. As indicated by the arrow (in Figure 3.6 at Cu $2p_{3/2}$ peak), the presence of native oxide significantly reduces after Cu TA and Cu EP when compared to Cu. There is also an increase in relative intensity of Cu

2p after thermal annealing and electropolishing indicating that the signal intensity is dominated by Cu rather than the Cu metal oxide. The quantification of Cu and O is shown in the inset of Figure 3.6. The relative quantity of oxygen present in the form of metal oxide (CuO or Cu_2O) on the surface decreases after thermal annealing and disappears below the detection limit of XPS ($\approx$ 1 part per thousand) with electropolishing. It is expected that the Cu surface after electropolishing forms a native oxide on the surface. Yet, the presence of these trace oxides were not detected by XPS indicated the oxide concentrations were at or below the XPS detection limit.

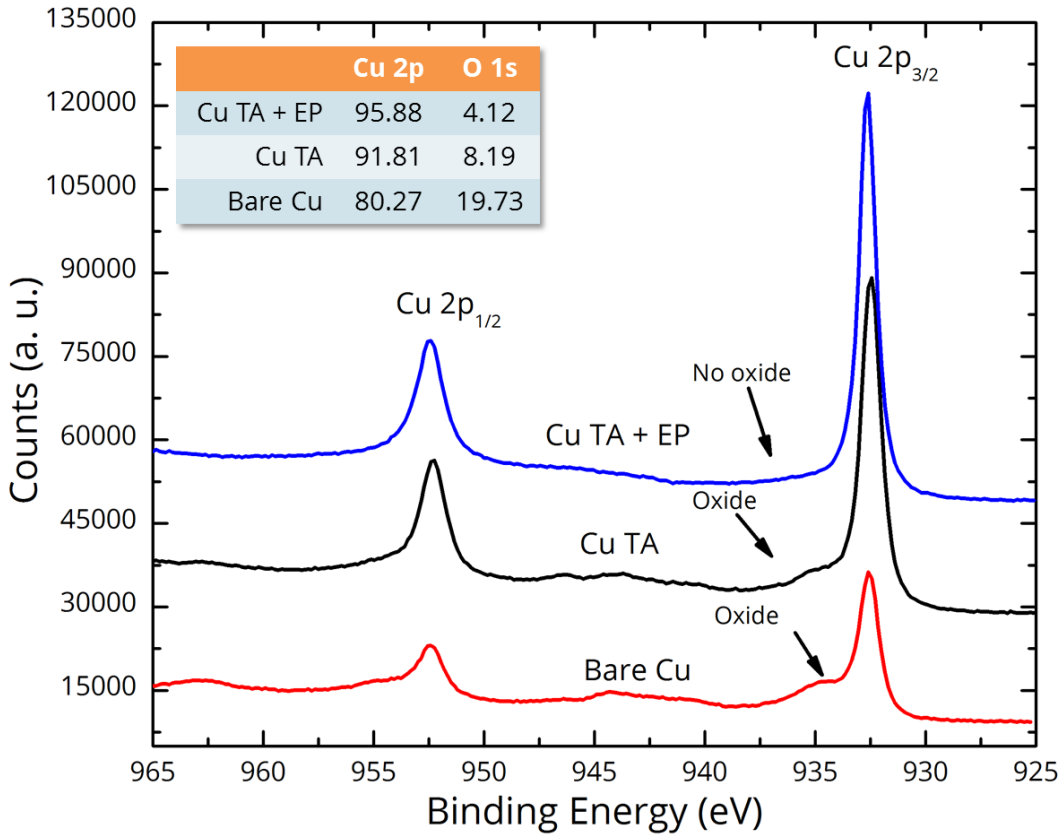

Figure 3.6: High resolution X-Ray Photoelectron Spectroscopy of Cu 2p. The inset shows the relative composition of Cu and O on the surface. The XPS signal associated with the thinning of native oxide (shown using an arrow) below the XPS detection limit after Cu thermal annealing and electropolishing of thermally annealed Cu sample.

From AFM and XPS analysis, it is understood that a two-step thermal anneal followed by electropolishing makes the Cu surface much more suitable for the CVD growth of h-BN by smoothing the surface and thinning the native oxide. Despite the favorable surface created by TA followed by electropolishing, etch pits occur

consistently with concentrated H_3PO_4. Therefore, it is important to devise a method to remove etch pits, as they may act as undesirable nucleation sites or impede the lateral growth of h-BN, using additives as reported in the literature [65, 66, 67, 68].

3.4 Electropolishing using the two-additive process

A two-additive electrolyte is used to reduce oxygen bubbling which causes etch pits. The electrolyte is prepared from concentrations reported in the literature [64, 65, 66, 67, 68, 70]. Voltammetry is performed to study the I-V relationship of the compound electrolyte. The two-additives chosen, Ethylene Glycol (EG) and glacial acetic acid, are expected to reduce the overall electrolyte conductivity when combined with concentrated H_3PO_4 electrolyte as reported in the literature. Voltammetry is performed on additives individually i.e. 50% EG + 50% concentrated H_3PO_4 and 50% Acetic Acid + 50% concentrated H_3PO_4, all by volume, to confirm the expected lowering of electrolyte conductivity prior to creating the two-additive compound electrolyte. The expected non-linear voltammetric curve is also observed (see Figure 3.7). However, the three distinct regions make a less pronounced appearance with the addition of additives. The inflection voltage (voltage of gas evolution) is higher with the presence of additives and the voltammetric curve is also observed to stretch (in the voltage direction of the plot). 2.3 V was chosen as an appropriate value ($\approx$ center of the dissolution region) for electropolishing potential after observ-

ing the voltammetric curve of the compound electrolyte. Initial investigations on electropolishing time demonstrated that for times in excess of 30 minutes the Cu foil became so thin that it was easily torn during the sample unloading process after electropolishing.

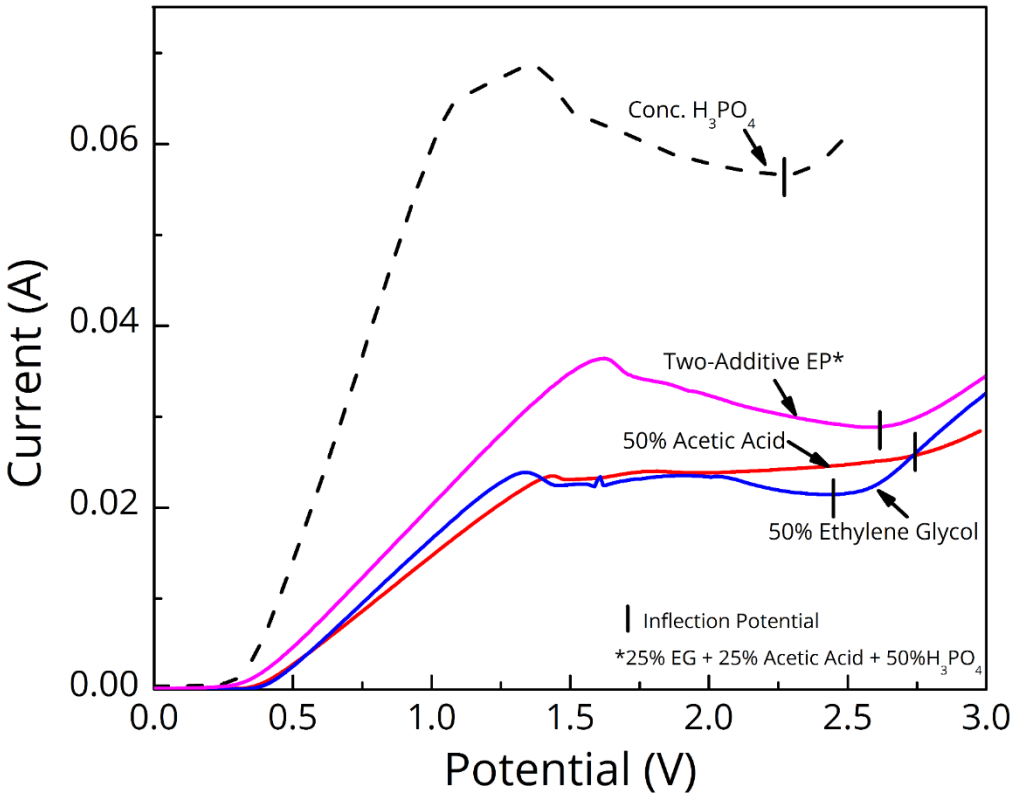

Figure 3.7: Voltammetry of various additives in standard electrolyte (concentrated H_3PO_4). The addition of additives reduces the current when contrasted with concentrated electrolyte indicated using a dashed curve.

The surface of the two-additive electropolished Cu (Cu EP-2) and Cu after thermal annealing (Cu TA EP-2) is assessed using AFM and SEM shown in Figure 3.8 and 3.11, respectively. The AFM analysis shows that the thermally annealed two additive electropolishing causes smoothing of the surface (Figure 3.8a). The

height image of Cu TA EP-2 shows almost no variations (Figure 3.8a) while the Cu EP-2 grains become visible in Cu after electropolishing under two additive process (shown in Figure 3.8c). The phase image does not show any variation for Cu TA EP-2 (as observed in Figure 3.8b), which is expected to be of single crystallographic orientation as discussed earlier. However, the Cu EP-2 shows phase variations, which is evident by the various crystallographic orientations of the grains as visible in the height and phase images (shown in Figure 3.8 c and d).

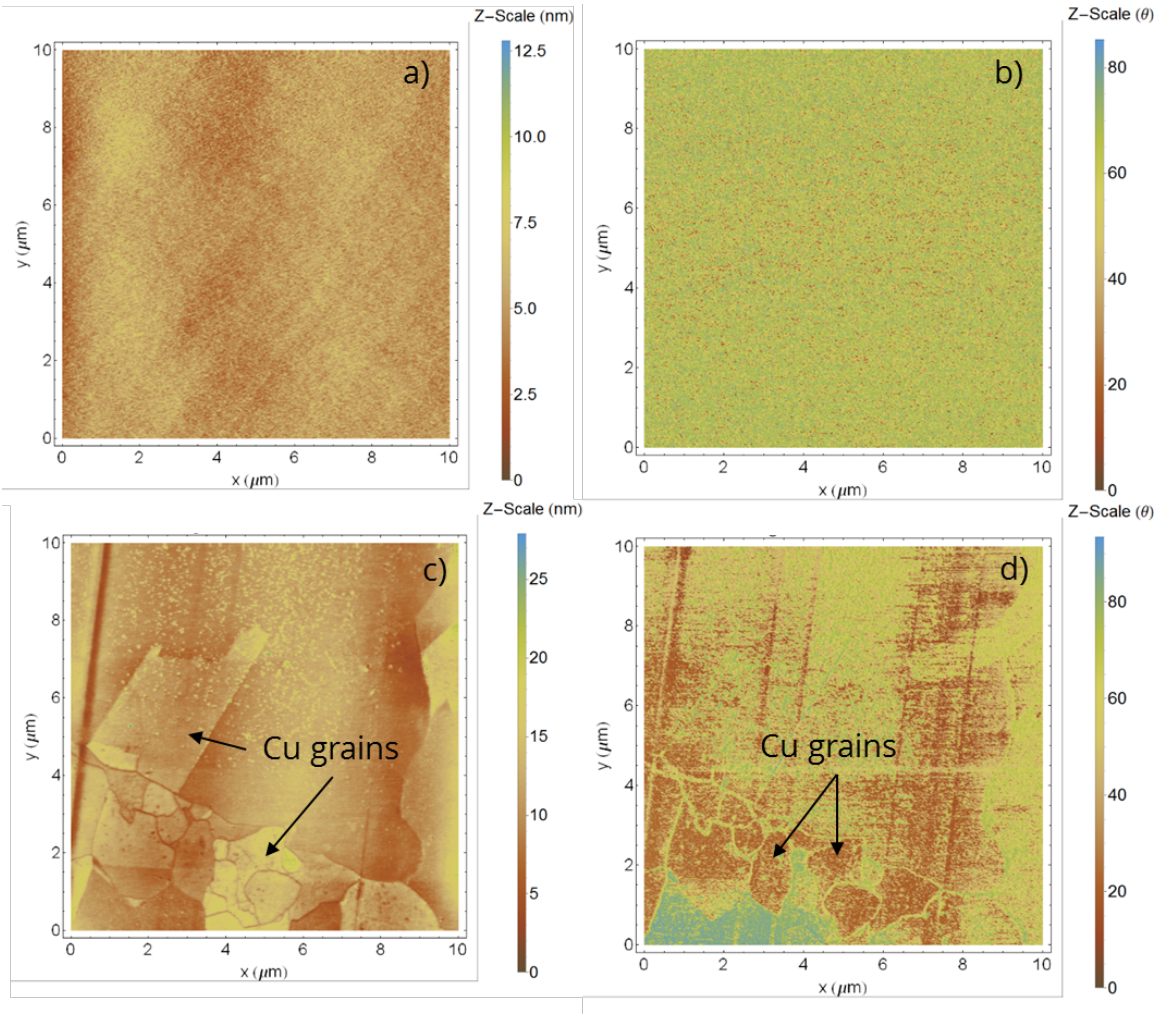

Figure 3.8: Tapping mode AFM height and phase images of Cu TA EP-2 (a and b, respectively) and Cu EP-2 (c and d, respectively) with the two additive electropolishing.

To further explore and quantify the evolution of surface morphological features caused by the importance of the two-step thermal anneal two-additive electropolishing approach, roughness measurements using an AFM have been performed. The root mean square (RMS) roughness is given by: $x_{rms} = \sqrt{\frac{1}{n}(x_1^2 + x_2^2 + x_n^2)}$. The roughness measurement is compared with a two-step TA and electropolishing non-

additive approach to illustrate the roughness (Figure 3.9). The surface roughness of the Cu foil is expected to decrease after thermal annealing ($\approx$ 6.67 nm) from its original state ($\approx$ 19.4 nm). However, the roughness after thermal annealing ($\approx$ 6.67 nm) is still too rough in comparison with the 2-dimensional nature of the h-BN grown which is reported to be 0.42 nm on Cu surface [4]. The RMS roughness across three different electropolishing times of the TA Cu foil as previously shown in Figure 3.5 are assessed. Electropolishing reduces the roughness from the TA state eventually reaching a plateau after which no significant smoothing happens locally (see in Figure 3.9). Since the main issue with the standard electropolishing procedure is the etch pits, the additives are utilized to eliminate the etch pits. Therefore, it is necessary to compare the two-additive process to the standard electropolishing procedure to confirm that electropolishing is indeed taking place and that the roughness is unaffected. The roughness measurements indicate that the two-additive electropolishing process reduces the roughness even further to $\approx$ 1.2 nm (RMS roughness measured across three different regions from the same AFM scan). The peak-to-peak line profiles (shown in Figure 3.10) are also within the roughness value of 1.1 nm. The low roughness paired with removal of etch pits make the two-additive process extremely attractive for the growth of two-dimensional materials.

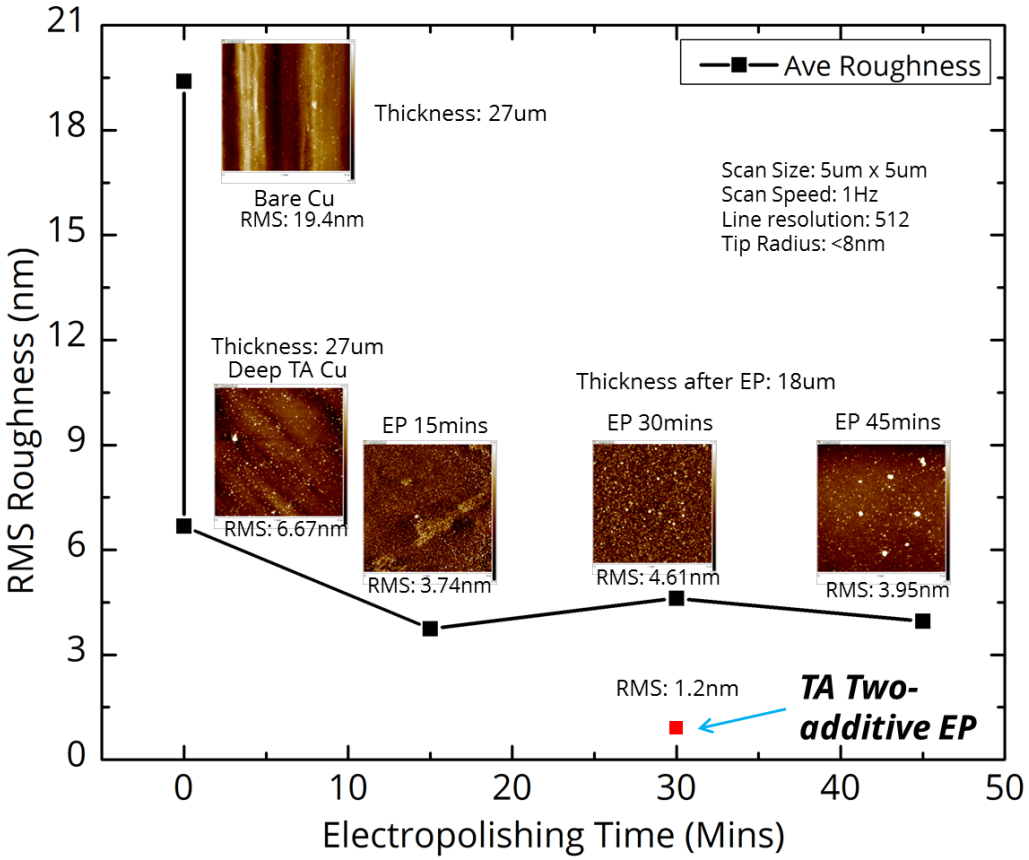

Figure 3.9: Average RMS roughness evolution after each processing step of Cu surface. Electropolishing decreases the roughness after thermal annealing but reaches a plateau. The red square shows the data point of average RMS roughness of Cu TA EP-2.

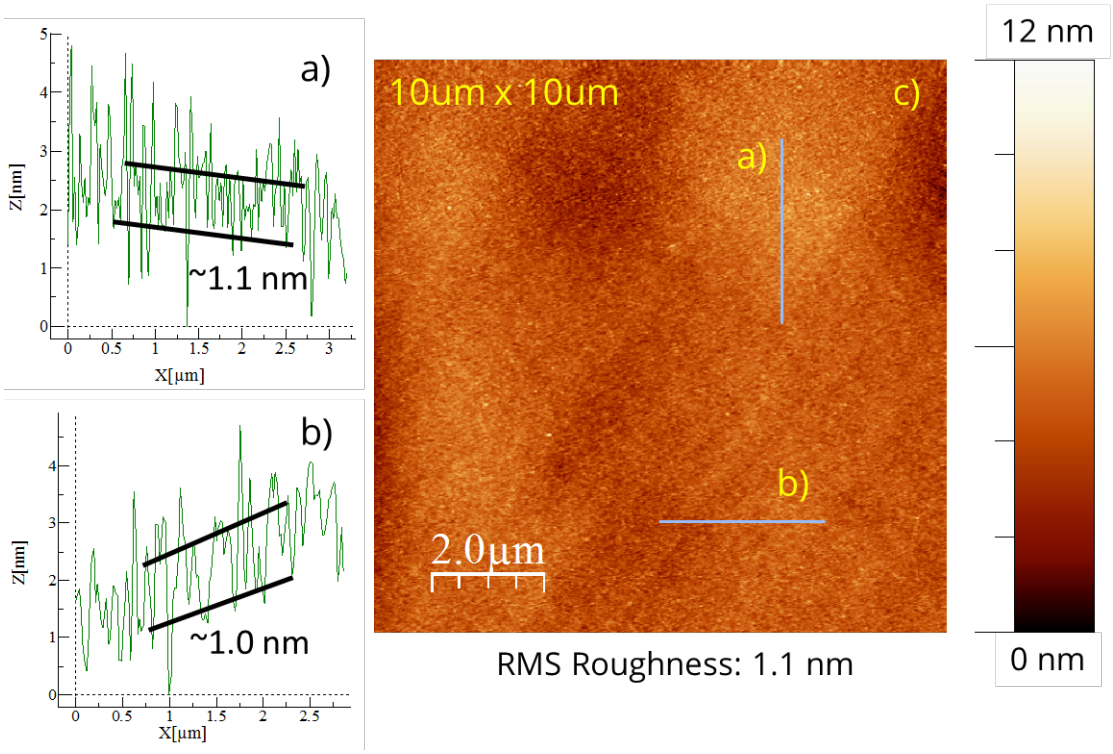

Figure 3.10: Line profiles of AFM height image of Cu TA EP-2 shown in a) and b). The RMS roughness measured across the whole 10 µm × 10 µm scan is ≈ 1.1 nm.

An SEM analysis of the Cu surface is performed to study the amount of surface planarization, qualitatively, as shown in Figure 3.11 for Cu and Cu TA with standard electropolishing and the two-additive approach for comparison. The surface of Cu shows significant etch pits with standard electropolishing process (indicated by arrows in Figure 3.11a). The etch pits are also visible on Cu TA on standard electropolishing process (Figure 3.11b) but are significantly less numerous in comparison to Cu with standard electropolishing process. The etch pits disappear when two-additive electropolishing process is used for both Cu and Cu TA attesting a cleaner electropolishing process. The rolling lines are faintly visible on Cu as indicated by the direction lines on the SEM image (Figure 3.11c). The thermally annealed two-

additive electropolishing process (Figure 3.11d) shows complete planarization of the surface without the existence of any etch pits, waviness or rolling lines and indeed confirms that the two-additive process is effective in both smoothing and planarizing the Cu surface making it suitable for CVD growth of two-dimensional materials.

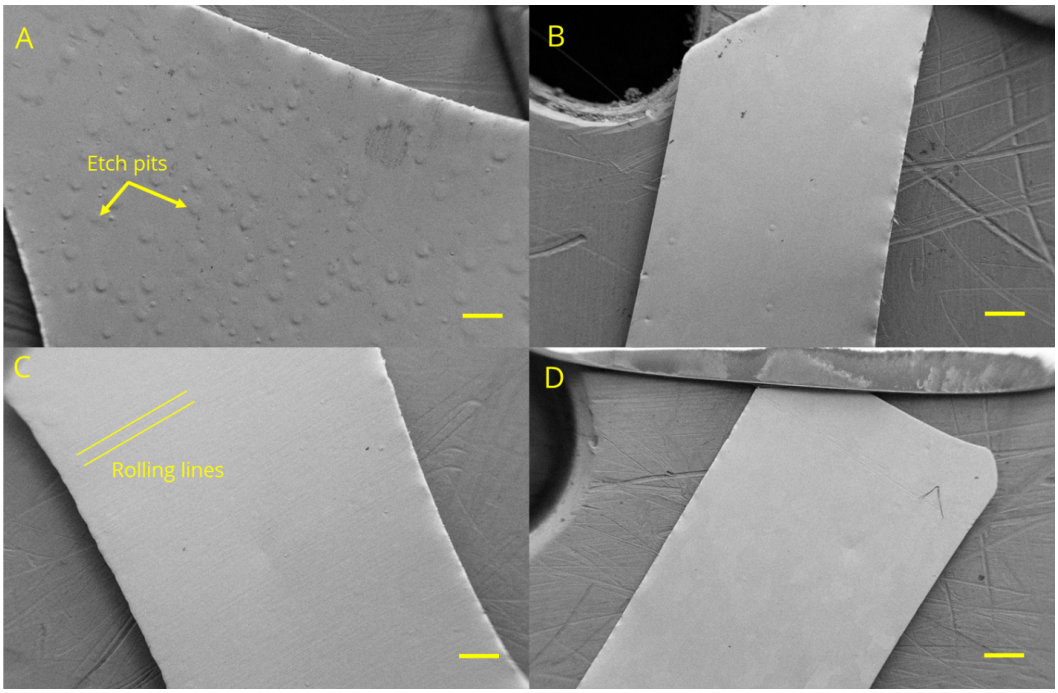

Figure 3.11: SEM images of Cu TA with standard electropolishing and two-additive electropolishing. a and b are Cu samples without and with thermal annealing electropolished using the standard non-additive electropolishing. c and d are Cu samples without and with thermal annealing using the two additive electropolishing process. The scale bar is 400 μm and the magnification is 22x.

CHAPTER 4

Growth of hexagonal boron nitride on electropolished Cu foils

In this chapter, h-BN on electropolished copper grown using a CVD process and the implications of the substrate on nucleation and growth will be discussed. Two independent growth studies were performed: 1) h-BN on thermally annealed Cu (Cu TA) and on thermally annealed electropolished (without additives) Cu (Cu TA EP), 2) h-BN on two-additive electropolished Cu, with and without thermal annealing prior to electropolishing (Cu TA EP-2 and Cu EP-2, respectively) along with a new control sample (Cu TA-2) identical to the first study. All the Cu samples were annealed *in situ* prior to growth of h-BN. The *in situ* annealing was performed in an H_2-N_2 environment at 1030°C for 5 hours. For the first study, the growth was done for 20 minutes at 1030°C and for the second study; the growth was done for 25 minutes at 1030°C. The growth time is limited so that the crystal size and distribution can be observed and the step height of h-BN crystal can be measured.

The precursor for the CVD growth is ammonia borane (H_3NBH_3) flowing downwards in a vertical tube furnace at 1.1 psig. The Cu samples were supported by perforated pyrolytic boron nitride crucible. After the growth process, SEM and FTIR were performed on all samples to assess the lateral growth of h-BN and to confirm that h-BN was grown on Cu, respectively. AFM was performed only on the control sample and the two-additive thermally annealed electropolished sample from the second growth study to assess the relationship between the Cu substrate morphology and h-BN nucleation.

4.1 Growth of h-BN

4.1.1 h-BN on non-additive electropolished Cu

Growth of h-BN was initially performed on Cu TA and on non-additive electropolished Cu TA samples (Cu TA EP), where Cu TA was used as control sample. SEM images were taken to ascertain the h-BN crystal size and count. The SEM images of Cu TA (control) and Cu TA EP samples, a local view ($\approx 10\mu m$) and a global view ($\approx$ 50 μm) are shown in Figure 4.1. The nucleation sites, where crystal budding occurs, are the bright dot-like spots as indicated in the SEM images (Figure 4.1 a, b, and d). These bright spots are understood as nucleation sites as the spots are located in the center of h-BN crystal and h-BN crystal nucleate where these bright spots are located on the Cu surface. The h-BN crystals are the darker triangular regions and is indicated by the dashed outline on the SEM images in Figure 4.1

a and b. The triangular shape of the h-BN crystal on Cu is also reported in the literature [4].

The reduction in nucleation density can be immediately observed from SEM images (Figure 4.1) when comparing a with b, and c with d. The nucleation site density is $\approx$ 100 sites on Cu TA and $\approx$ 68 sites on Cu TA EP in 10 μm $\times$ 10 μm SEM image (Figure 4.1 a and b). The nucleation sites, bright spot-like features, appear to be much larger on the electropolished sample than on the thermally annealed sample. This is immediately observed when comparing a with b and c with d in Figure 4.1. The bright spots are almost invisible in Cu TA global view (Figure 4.1c) but are more conspicuous on Cu TA EP global view (Figure 4.1d). The reason for a dimensionally larger nucleation site after electropolishing is not understood and may require further studies (discussed in chapter 6). The crystal size is also observed to be significantly larger on Cu TA EP than on the Cu TA as shown in Figure 4.1b and Figure 4.1a, respectively. The triangular h-BN crystal sizes are $\approx$ 1 μm in Cu TA and $\approx$ 2 μm in Cu TA EP where the indicated measurements are the sizes of each side of the triangular crystal. This indicates that electropolished Cu surface is having an immediate effect on increase in h-BN crystal size.

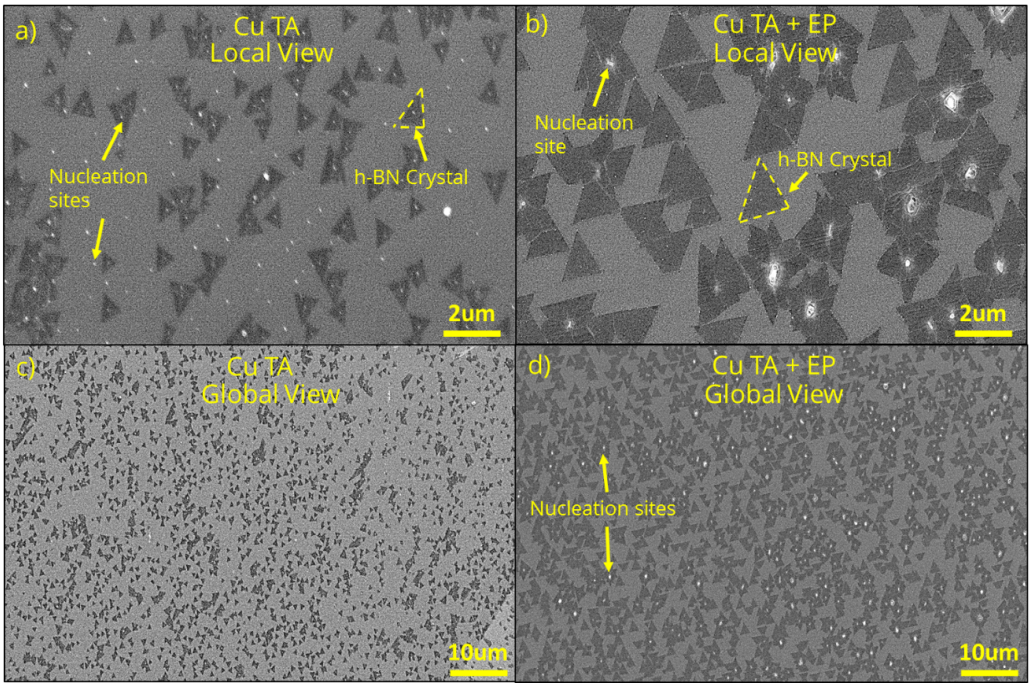

Figure 4.1: SEM images of h-BN grown on thermally annealed Cu foil (control sample) and electropolished Cu foil. The dashed outline shows the h-BN crystals and the bright dot-like structures are the nucleation sites.

ATR-FTIR spectroscopy confirms the growth of h-BN on Cu. Figure 4.2 shows the signature absorbance peak of h-BN at $\approx$ 824 cm^{-1} for both Cu TA (control sample) and the Cu TA EP sample [44]. The electropolished sample shows a higher peak intensity which can be ascribed to the larger h-BN crystal as shown in SEM images. This is because the intensity is proportional to the overall concentration of h-BN on the surface [74]. Despite the density of crystals being fewer in Cu TA EP, the larger flake size on Cu TA EP gives a higher areal coverage and contributes to the increase in peak intensity. The narrow peak, measured by the FWHM ($\approx$ 5 wavenumbers), also confirms that the h-BN crystals on Cu TA and Cu TA EP are

morphologically uniform [74].

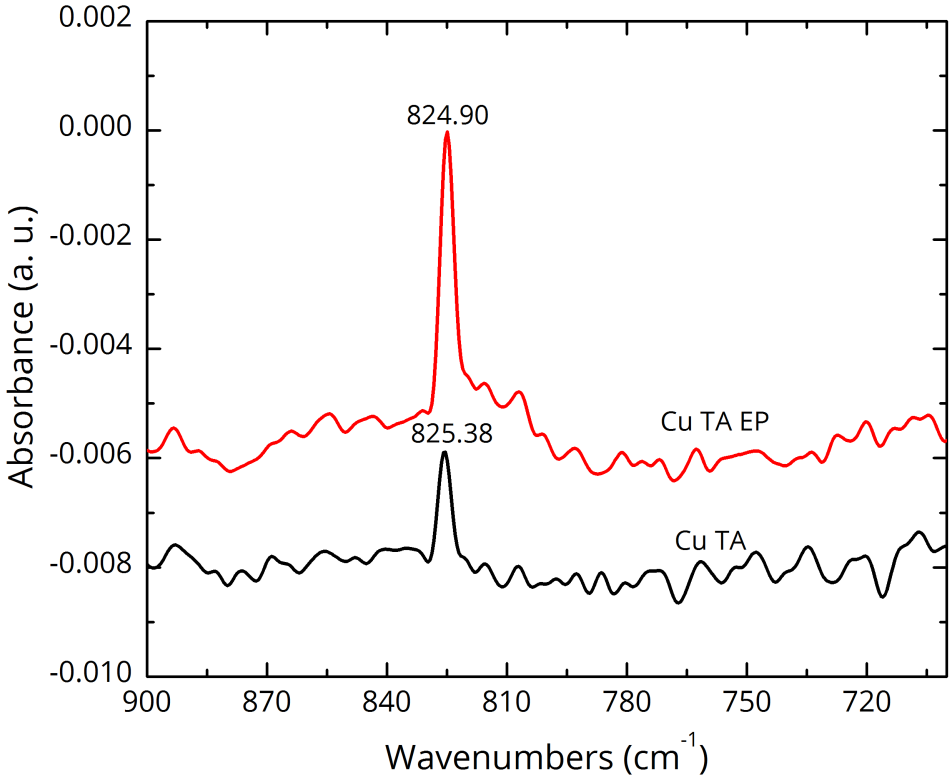

Figure 4.2: Attenuated Total Reflectance Fourier Transform Infrared (ATR-FTIR) spectroscopy of thermally annealed Cu and electropolished Cu using the standard electrolyte.

4.1.2 h-BN on two-additive electropolished Cu

h-BN is also grown on the two-additive electropolished samples with and without thermal annealing along with a thermally annealed Cu which acts as the control sample. SEM and FTIR are performed on all three samples after growth of h-BN to characterize the h-BN crystals and validate the material grown on the Cu surface,

respectively. In agreement with the previous results on Cu, fewer nucleation sites are observed along with larger h-BN crystals on the electropolished samples as shown in Figure 4.3 a and b. The nucleation site density is $\approx$ 210 sites for Cu TA-2, $\approx$ 12 sites for Cu TA EP-2, and $\approx$ 14 sites for Cu EP-2 in the $\approx$ 20 μm SEM image in Figure 4.3. The size of the h-BN crystal is measured to be $\approx$ 1 μm for Cu TA-2, $\approx$ 3 μm for Cu TA EP-2 and $\approx$ 4 μm for Cu EP-2.

Of the three surfaces compared, Cu TA EP-2 shows the fewest nucleation site density while Cu TA-2 shows the largest density. The nucleation sites can be located by bright white spots on the SEM images and appear to be randomly dispersed on the Cu surface. In Cu TA EP-2, growth appears to take place on a larger nucleation site as indicated with an arrow in Figure 4.3b. While there are other areas on Cu TA EP-2 where nucleation sites are visible but no growth takes place. In Figure 4.3a, growth on Cu EP-2 is much more different in that the h-BN crystal size is the largest of the three Cu surfaces (Cu TA-2, Cu EP-2 and Cu TA EP-2). As the two-additive electropolishing selectively dissolves the high regions on the Cu surface, the grains and grain boundaries are clearly visible on Cu EP-2. h-BN crystals appears to be located at or very close to the grain boundaries indicating that the grain boundaries play a role in either assisting nucleation or acting as nucleation site. This is readily observed on Cu EP-2 (Figure 4.3a), where the adjacent Cu grains can be identified by slightly different contrast and that the h-BN crystals are closely located at the Cu grain boundaries indicated by the red dashed line in Figure 4.3a. As thermal annealing enlarges the Cu grains (Cu grain size are $>$ 100 μm in size), the origin of h-BN nucleation cannot be immediately ascertained. Surface defects, such as step

edges, on Cu surface appear after thermal annealing (discussed in chapter 3) and they can potentially act as nucleation sites. Therfore, a scanning probe microscopy (SPM) technique such as the AFM is used to relate Cu surface morphology and origin of growth of h-BN crystals discussed in section 4.2. The h-BN crystal is also observed to merge into adjacent h-BN crystals in all the samples indicating continuity of crystal growth and crystal enlargement. Crystal merging is indicated by an arrow in Figure 4.3 a and b, and using a red square in Figure 4.3c.

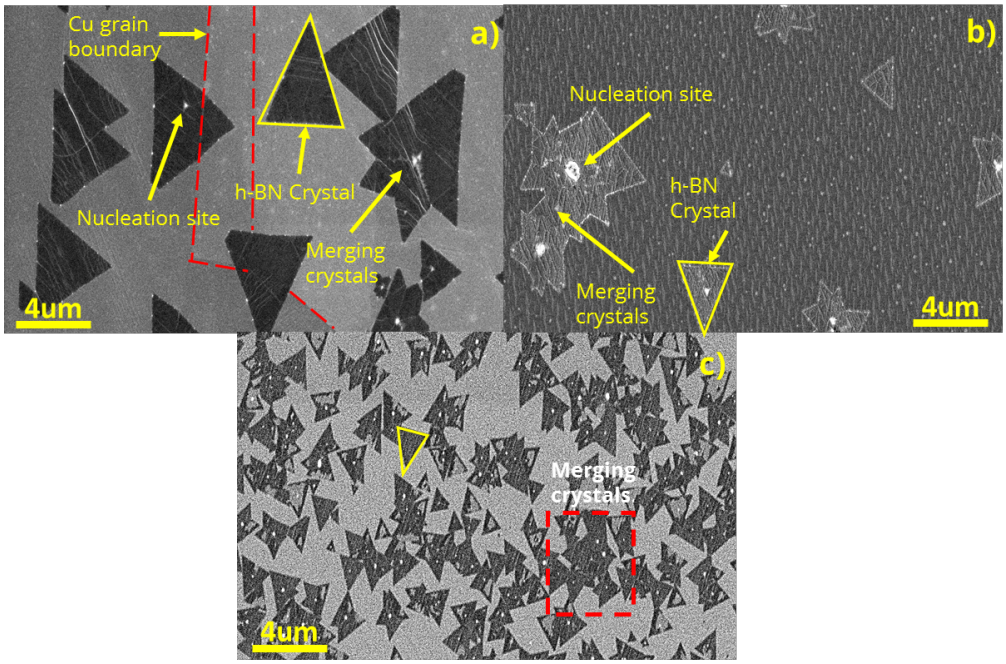

Figure 4.3: SEM of h-BN crystals grown on a) electropolished Cu (Cu EP-2) and b) thermally annealed electropolished Cu (Cu TA EP-2) and c) thermally annealed Cu TA-2. The h-BN crystals are indicated by triangular outline in a, b, and c. h-BN crystals merging is indicated in a) and b). The red dashed square shows crystal merging in c). The red dashed line in a) shows the location of Cu grain boundaries.

FTIR is performed on all three samples showing the characteristic h-BN peak

(shown in Figure 4.4) at $\approx$ 824 cm^{-1} [44]. Unlike the FTIR results discussed in Figure 4.2, the FTIR results of the growth of h-BN on two-additive electropolishing Cu are varying significantly. First, observation is that the peaks of h-BN on Cu EP-2 are not as intense as Cu TA EP-2 and Cu TA-2 and second, all the peaks are actually located at $\approx$ 820 cm^{-1}. The intensity can be attributed to fewer h-BN crystals in Cu EP-2 and Cu TA EP-2 than on Cu TA-2 despite h-BN being much larger in the former two samples. The peak areas are calculated by peak fitting using Origin Pro, which shows that the peak areas are 0.02137, 0.07719 and 0.03405 for Cu EP-2, Cu EP TA-2, and Cu TA-2, respectively. EP TA-2 has higher peak area than Cu TA-2 as calculated from the peak fit, where the peak intensity and area is proportional to the areal coverage of h-BN on the surface. The peaks of h-BN on Cu EP-2 and Cu TA EP-2 are much broader than on Cu TA-2, where the FWHMs are: $\approx$ 6 cm^{-1}, $\approx$ 10 cm^{-1} and $\approx$ 4 cm^{-1} for Cu EP-2, Cu TA EP-2, and Cu TA-2, respectively. The reason for wider peaks is not understood at this point along with the location of peak at $\approx$ 820 cm^{-1}.

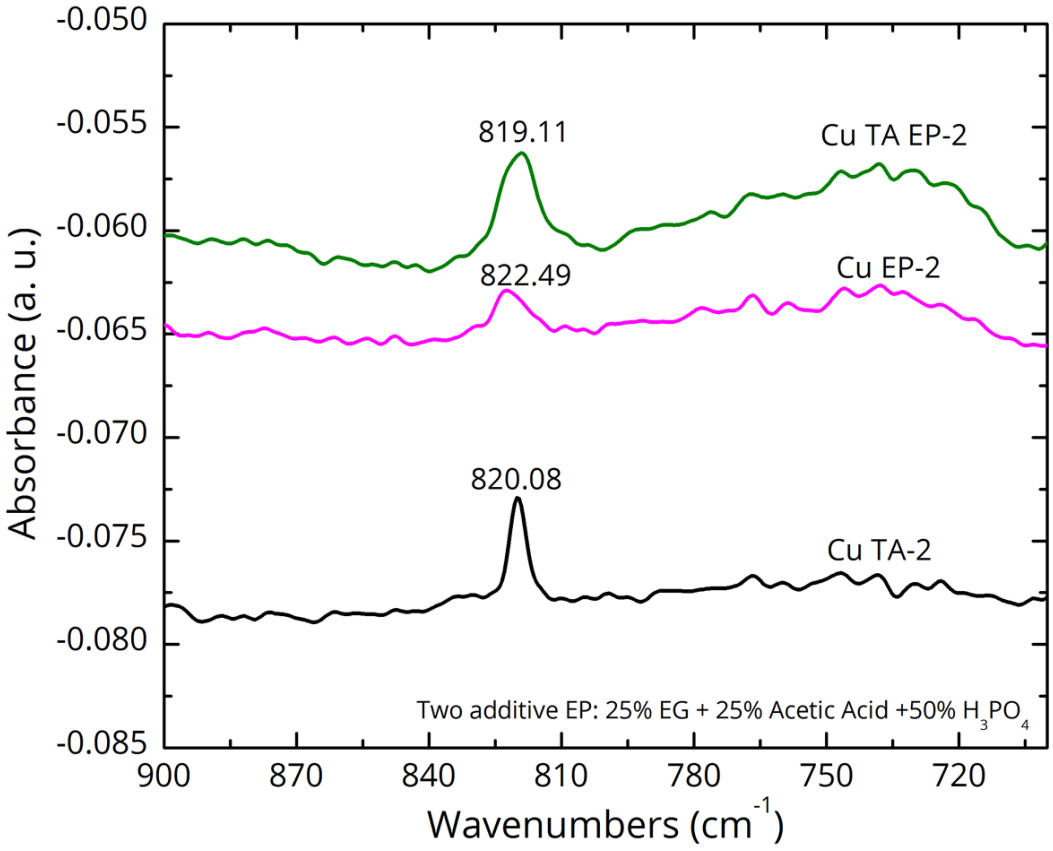

Figure 4.4: ATR-FTIR of h-BN on Cu TA EP-2, Cu EP-2 and Cu TA (top to bottom).

4.2 Surface morphology of h-BN on Cu surface

Tapping mode atomic force microscopy (TM-AFM) was performed on h-BN on the samples to determine the thickness of the growth film and to identify the location of h-BN crystal growth on Cu TA-2 and Cu TA EP-2. The latter is chosen as the surface is measured to be very smooth and free of etch pits that occurs with the standard non-additive electrolyte. Therefore, the AFM of h-BN on Cu surface can be more easily studied and contrasted with Cu TA-2, the control sample. Phase

images are also simultaneously obtained to identify the h-BN crystals on Cu surface. Figure 4.5 shows a summary of AFM results. Step edges and hump-like oblique protruding features ($\approx$ 1 μm wide and $\approx$ 3 μm long) are observed on the Cu TA-2 and Cu TA EP-2, respectively (Figure 4.5a and Figure 4.5c). Because of the features on Cu surface that dominate the height, h-BN is nearly invisible from the AFM height images. However, the phase image clearly shows a contrast between Cu foil, h-BN and also the nucleation site (discussed later). h-BN is observed to grow on prominent surface features, such as step edges on Cu TA-2 and hump-like features on Cu TA EP-2, but not on flatter regions of Cu TA EP-2, indicated in Figure 4.5c and Figure 4.5d. As the Cu TA-2 surface is dominated by step edges, there are no flat regions, and the growth appears to be at the step edges. The h-BN crystal sizes are observed to be much larger on Cu TA EP-2 than Cu TA-2 and there are fewer nucleation sites and h-BN crystals on Cu TA EP-2 than on Cu TA-2.

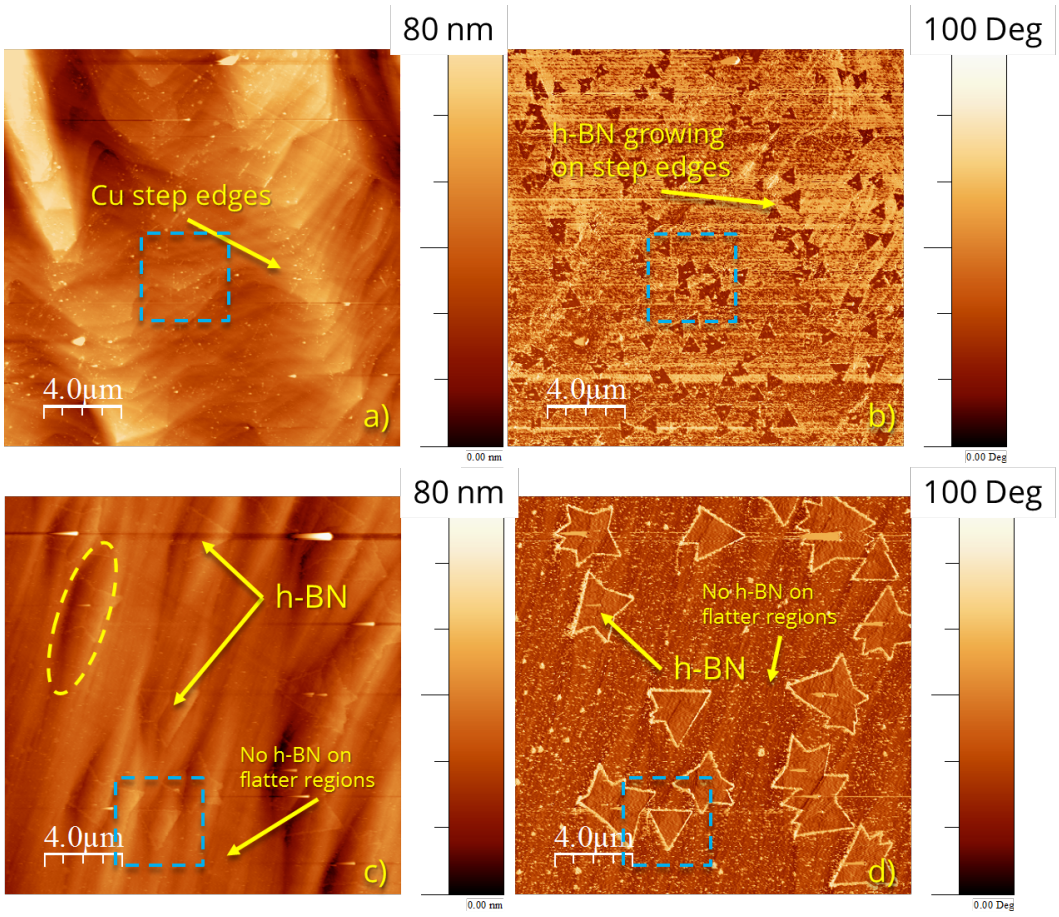

Figure 4.5: Tapping mode AFM of h-BN on Cu TA (top) and Cu TA EP-2 (bottom). a) and c) are height images of Cu TA and Cu TA EP-2, respectively and b) and d) are phase images of Cu TA and Cu TA EP-2, respectively. The AFM scan size in 20 µm × 20 µm. The blue dashed squares are 5 µm × 5 µm AFM scans shown in Figure 4.6 and Figure 4.7. The dashed yellow oval indicated in c) shows the hump-like oblique protruding feature on Cu TA EP-2 surface is ≈ 1 µm wide and ≈ 3 µm long.

4.2.1 Morphology of h-BN on Cu TA-2

A smaller 5 μm × 5 μm AFM scan was obtained to get a clearer understanding of h-BN crystals on Cu TA (shown in Figure 4.6). h-BN growth appears to be initiating on a step edge and the growth spreads laterally across adjacent steps. This conclusion can be made by observing and identifying a h-BN crystal on the phase image and locating the same h-BN crystal in the corresponding region on height image, where the step edges are prominently observed. The nucleation sites are also visible both on height and phase images. As discussed earlier in chapter 3 on potential nucleation sites, AFM results after the growth of h-BN confirm that these spike-like (or spot-like in 2D representation) are indeed nucleation sites. The dimensions of the potential nucleation site which is also discussed in chapter 3, is similar to the one shown in Figure 4.6c. The height of the nucleation site is ≈ 58 nm while the diameter is around ≈ 220 nm as measured from the AFM line scan shown in Figure 4.6a. As discussed in section 3.2 on potential nucleation sites prior to growth, the nucleation site which is at the center of the h-BN crystal appears to have a different material composition. The phase image (Figure 4.6b) shows that the phase contrast of the nucleation site is neither similar to h-BN nor Cu. The nucleation sites vary in height and diameter but are tens of nanometers in height and hundreds of nanometer in diameter. In general, the nucleation sites are much larger in height than any of the Cu surface inhomogeneities as is evident in Figure 4.6 height and phase images of both Cu TA-2 and Cu TA EP-2 where the nucleation sites can be identified from the oversaturated spots on the AFM images.

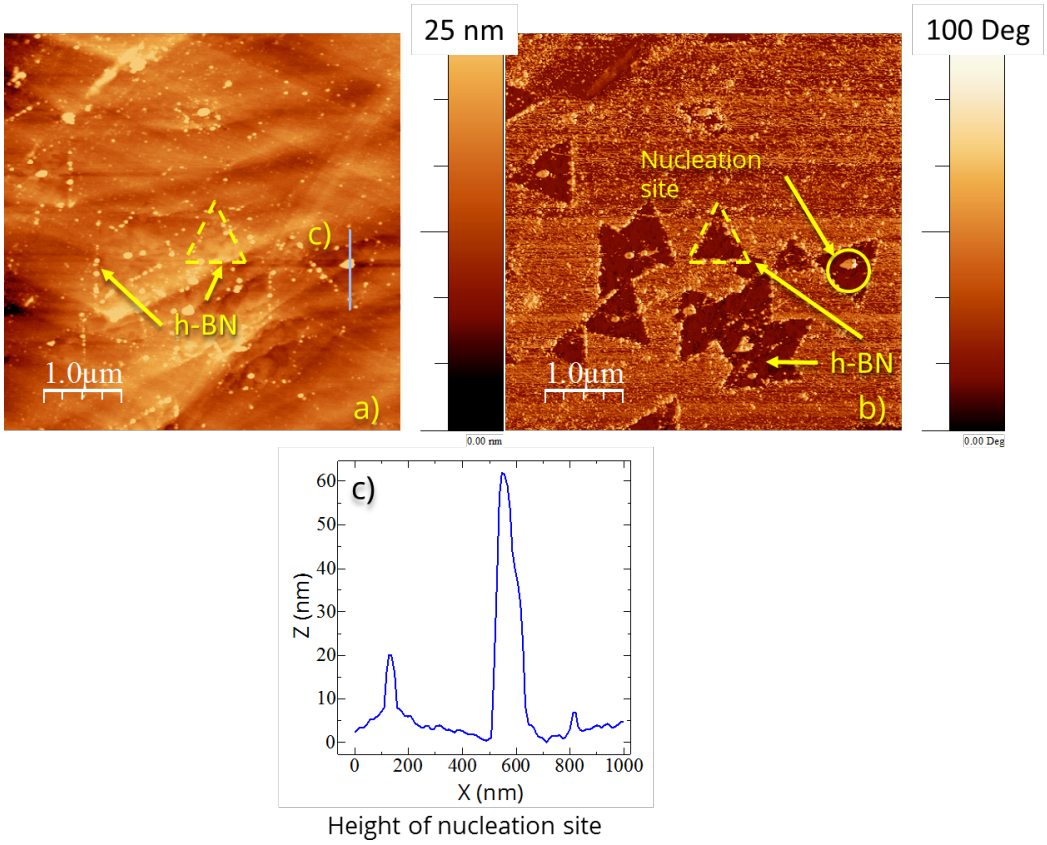

Figure 4.6: A 5µm × 5 µm AFM scan of h-BN on Cu TA. A) Height, b) Phase. Line scan of the nucleation site in a) is shown in c).

4.2.2 Morphology of h-BN on Cu TA EP-2

A smaller 5µm × 5 µm AFM is also performed on Cu TA EP-2 which is shown in Figure 4.7. A clear difference is that the h-BN crystal size is much larger on Cu TA EP-2 surface than on Cu TA and there are fewer nucleation sites as well as fewer crystals on Cu TA EP-2. The thickness of the h-BN crystal is measured from line scan from the AFM height image as shown in Figure 4.7d as an example. The average thickness, measured across three different h-BN crystals, is ≈ 0.46 nm

which confirms that the h-BN crystal is a single monolayer and is in good agreement with reported value (0.42 nm) on Cu substrate [4]. This measurement could not be made on Cu TA-2 foil because of the inhomogeneity of step edges affect the height measurement. By comparing the height and the phase images, the shape of the h-BN crystal appears to be influenced by the shape of Cu surface inhomogeneities. This is more acutely evident from the height image of Cu TA EP-2 (Figure 4.7a), where the h-BN crystal growth nucleates on the hump-like features on the surface and gradually spreading over regions past the hump-like features.

Similar to Cu TA-2, nucleation sites are also observed from the AFM height and phase image as shown in Figure 4.7 a and b. The dimensions of nucleation site shown in Figure 4.7c is $\approx$ 48 nm in height with a diameter of $\approx$ 250 nm, which is similar to the one shown in Figure 4.6c. It appears that the dimensions of the nucleation sites are not affected by the electropolishing process after thermal annealing but the density is reduced i.e. electropolishing is dislodging the potential nucleation sites from the Cu surface which are either created or enhanced by thermal annealing.

As observed from the phase image (Figure 4.7b), the outline of the h-BN crystal appears to be of a different contrast than h-BN or Cu but similar in contrast with nucleation sites. It is unclear from the AFM height or phase image if the outline is actually contaminant diffusing from the bulk during growth or debris agglomerating at the edges after growth of h-BN on Cu. This is also observed from AFM of h-BN crystals on Cu TA-2 (shown in Figure 4.6) but as the crystals are much smaller than on Cu TA EP-2, the outline is not readily resolved.

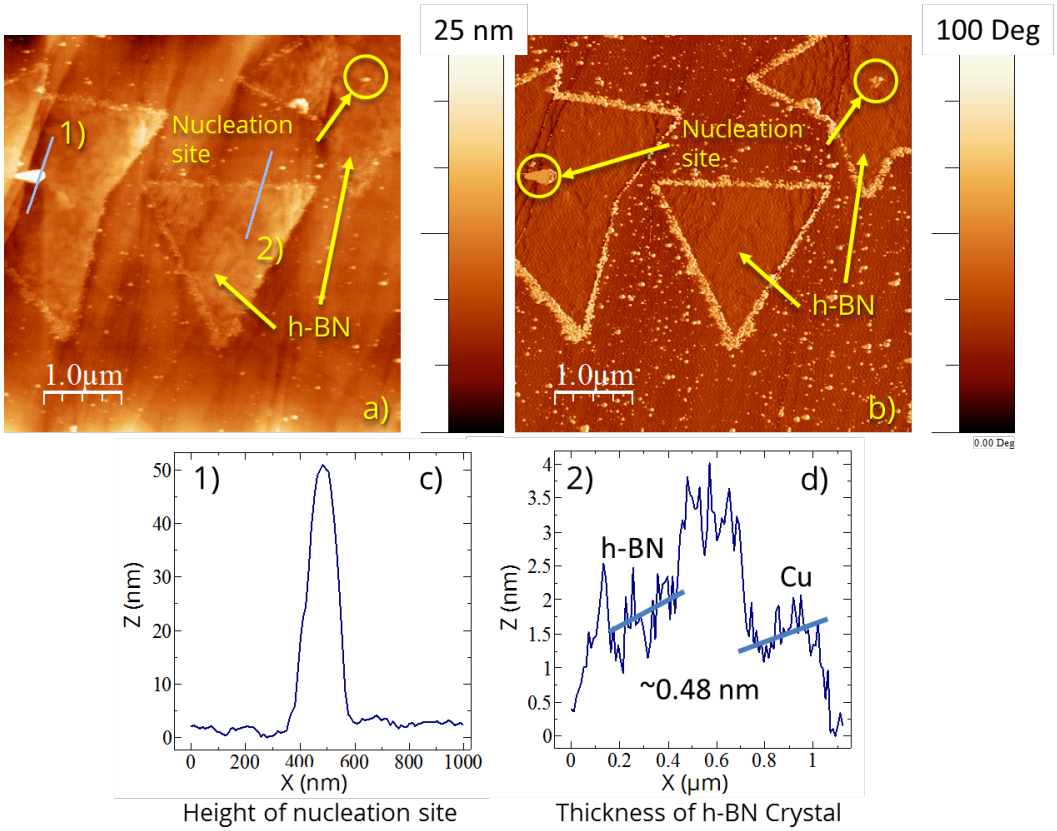

Figure 4.7: AFM surface morphology of h-BN on Cu TA EP-2. a) Height, b) Phase. Line scan of nucleation site and thickness of h-BN crystal shown as an example in c) and d), respectively. 1) and 2) on a) indicate the location from where the line scan is obtained. The lines drawn in d show the approximate region where the h-BN thickness is calculated. AFM scan size is 5 µm × 5 µm.

CHAPTER 5

Summary and conclusions

This work demonstrates that electrochemical polishing has an effect on the surface of copper foils which influences the growth of hexagonal boron nitride. The copper foil supplied by the vendor is shown to have the highest roughness ($\approx$ 19.4 nm) of all samples studied for this work, with macroscopic ($>$ 1 μm) and microscopic ($<$ 1 μm) surface inhomegenities and along with a native copper oxide. Thermal annealing in reduced environment changes the surface. The macroscopic and microscopic features are no longer observed and the native oxide is significantly reduced as shown using XPS. Thermal annealing also promotes Cu grain growth. However, AFM shows the existence of surface defects on the thermally annealed copper in the form of step edges. The roughness measurement of thermally annealed Cu surface is $\approx$ 6.67 nm. Electropolishing is utilized to reduce the surface defects arising during thermal annealing and the roughness is measured to be $\approx$ 4.8 nm. The standard non-additive electropolishing is shown to contain etch pits arising from the oxygen bubbling. A two-additive electrolyte was utilized to reduce oxygen evolution and consequently

pitting. The two-additive electropolishing is shown to remove the surface defects (step edges) observed after thermal annealing. The roughness for the two-additive electropolishing process is measured to be $\approx$ 1.1 nm. XPS of electropolished Cu shows that the native oxide on copper is reduced significantly below the detection limit (1 part per thousand) of XPS. AFM reveals the existence of spike-like features that are suggested to be potential nucleation sites. The dimensions of these spike-like features are measured to be tens of nanometers in height and hundreds of nanometers in width.

h-BN is grown on thermally annealed copper and thermally annealed electropolished copper. The growth results indicate that the nucleation site density has substantially reduced after electropolishing and the h-BN crystal size is enlarged observed using SEM. FTIR spectroscopy confirms the existence of h-BN. AFM is used to quantify the thickness ($\approx$ 0.48 nm) of h-BN on Cu which is measured to be a monolayer. The dimensions of the nucleation sites is also obtained from AFM and are found to be similar to the spike-like features observed prior to growth. Therefore, it is understood that these spike-like features in fact are nucleation sites. The growth of h-BN is also observed to be located near other Cu surface defects (step edges on Cu TA and $\approx 1\ \mu m \times 3\ \mu m$ features on Cu TA EP-2).

In conclusion, electropolishing of Cu substrates has a positive effect on the growth of h-BN by increasing the size of crystals and reducing the nucleation sites. This work therefore establishes electropolishing as a technique that can be utilized to modify a Cu substrate for more controllable growth of two-dimensional materials, specifically hexagonal boron nitride.

CHAPTER 6

Future work

Despite demonstrating the effect of electropolishing on Cu surface and h-BN growth on Cu, there are several avenues for further experimentation. Three routes of studies can be initiated: 1) Electropolishing of Cu with recipes that are optimized for Cu foils using alternate additives which could lead to global planarization of Cu surface. 2) Studies with a goal to understand the composition and structure of the spike-like features using TEM to develop a relationship between the nucleation site and the h-BN crystal. 3) STM and UHV AFM can be used to study the surface morphology, including roughness, of the h-BN crystals which has implications for growth of graphene/h-BN heterostructures.

Bibliography

[1] B. Zhang, W. Lee, R. Piner, I. Kholmanov, Y. Wu, H. Li, H. Ji, and R. Ruoff, "Low-temperature chemical vapor deposition growth of graphene from toluene on electropolished copper foils.," *ACS Nano*, vol. 6, pp. 2471–6, Mar 2012.

[2] Z. Luo, Y. Lu, D. W. Singer, M. E. Berck, L. A. Somers, B. R. Goldsmith, and A. T. C. Johnson, "Effect of substrate roughness and feedstock concentration on growth of wafer-scale graphene at atmospheric pressure," *Chemistry of Materials*, vol. 23, 2011.

[3] I. Vlassiouk, P. Fulvio, H. Meyer, N. Lavrik, S. Dai, P. Datskos, and S. Smirnov, "Large scale atmospheric pressure chemical vapor deposition of graphene," *Carbon*, vol. 54, 2013.

[4] K. Kim, A. Hsu, X. Jia, S. Kim, Y. Shi, M. Hofmann, D. Nezich, J. Rodriguez-Nieva, M. Dresselhaus, T. Palacios, and et al., "Synthesis of monolayer hexagonal boron nitride on Cu foil using chemical vapor deposition.," *Nano letters*, vol. 12, pp. 161–6, Jan 2012.

[5] M. Groover, *Fundamentals of Modern Manufacturing: Materials, Processes, and Systems*. John Wiley & Sons, 2010.

[6] S. Kalpakjian and S. Schmid, *Manufacturing Engineering & Technology*. Pearson Education, 2013.

[7] S.-H. Kim, S. Z. Han, C. J. Kim, I.-Y. Hwang, and F. Yin, "Evolution of rolling textures of cold rolled copper foils," *MATERIALS TRANSACTIONS*, vol. 50, no. 3, pp. 537–543, 2009.

[8] P. Huang, C. Ruiz-Vargas, A. van der Zande, W. Whitney, M. Levendorf, J. Kevek, S. Garg, J. Alden, C. Hustedt, Y. Zhu, and et al., "Grains and grain boundaries in single-layer graphene atomic patchwork quilts," *Nature*, vol. 469, pp. 389–92, Jan 2011.

[9] G. Han, F. Gnes, J. Bae, E. Kim, S. Chae, H.-J. Shin, J.-Y. Choi, D. Pribat, and Y. Lee, "Influence of copper morphology in forming nucleation seeds for graphene growth," *Nano letters*, vol. 11, pp. 4144–8, Oct 2011.

[10] J. Cho, L. Gao, J. Tian, H. Cao, W. Wu, Q. Yu, E. Yitamben, B. Fisher, J. Guest, Y. Chen, and et al., "Atomic-scale investigation of graphene grown on Cu foil and the effects of thermal annealing," *ACS nano*, vol. 5, pp. 3607–13, May 2011.

[11] O. I. Sarajlic and R. G. Mani, "Mesoscale scanning electron and tunneling microscopy study of the surface morphology of thermally annealed copper foils for graphene growth," 2013.

[12] W. Tegart, *The electrolytic and chemical polishing of metals: in research and industry*. Pergamon Press, 1959.

[13] F. Schedin, A. Geim, S. Morozov, E. Hill, P. Blake, M. Katsnelson, and K. Novoselov, "Detection of individual gas molecules adsorbed on graphene," *Nature materials*, vol. 6, pp. 652–5, Aug 2007.

[14] Y. Dan, Y. Lu, N. J. Kybert, Z. Luo, and A. T. C. Johnson, "Intrinsic response of graphene vapor sensors," *Nano Letters*, vol. 9, no. 4, pp. 1472–1475, 2009.

[15] K. S. Novoselov, A. K. Geim, S. V. Morozov, D. Jiang, Y. Zhang, S. V. Dubonos, I. V. Grigorieva, and A. A. Firsov, "Electric field effect in atomically thin carbon films," *Science*, vol. 306, no. 5696, pp. 666–669, 2004.

[16] A. K. Geim and K. S. Novoselov, "The rise of graphene," *Nature Materials*, vol. 6, pp. 183–191, 2007.

[17] X. Wang, L. Zhi, and K. Mullen, "Transparent, conductive graphene electrodes for dye-sensitized solar cells," *Nano Letters*, vol. 8, no. 1, pp. 323–327, 2008. PMID: 18069877.

[18] K. Kim, Y. Zhao, H. Jang, S. Lee, J. Kim, K. Kim, J.-H. Ahn, P. Kim, J.-Y. Choi, and B. Hong, "Large-scale pattern growth of graphene films for stretchable transparent electrodes," *Nature*, vol. 457, pp. 706–10, Feb 2009.

[19] A. Geim, "Graphene: status and prospects," *Science*, 2009.

[20] J.-H. Chen, C. Jang, S. Xiao, M. Ishigami, and M. Fuhrer, "Intrinsic and extrinsic performance limits of graphene devices on SiO_2," *Nature nanotechnology*, vol. 3, pp. 206–9, Mar 2008.

[21] K. Watanabe, T. Taniguchi, and H. Kanda, "Direct-bandgap properties and evidence for ultraviolet lasing of hexagonal boron nitride single crystal.," *Nature Materials*, vol. 3, pp. 404–9, May 2004.

[22] C. Dean, A. Young, I. Meric, C. Lee, L. Wang, S. Sorgenfrei, K. Watanabe, T. Taniguchi, P. Kim, K. Shepard, and J. Hone, "Boron nitride substrates for high-quality graphene electronics," *Nature Nanotechnology*, vol. 5, no. 10, pp. 722–726, 2010.

[23] H. Wang, T. Taychatanapat, A. Hsu, K. Watanabe, T. Taniguchi, P. Jarillo-Herrero, and T. Palacios, "BN/graphene/BN transistors for rf applications," *Electron Device Letters, IEEE*, vol. 32, no. 9, pp. 1209–1211, 2011.

[24] G.-H. Lee, Y.-J. Yu, C. Lee, C. Dean, K. L. Shepard, P. Kim, and J. Hone, "Electron tunneling through atomically flat and ultrathin hexagonal boron nitride," *Applied Physics Letters*, vol. 99, no. 24, 2011.

[25] L. Britnell, R. Gorbachev, R. Jalil, B. Belle, F. Schedin, M. Katsnelson, L. Eaves, S. Morozov, A. Mayorov, N. Peres, and et al., "Electron tunneling through ultrathin boron nitride crystalline barriers," *Nano letters*, vol. 12, pp. 1707–10, Mar 2012.

[26] K. K. Kim, A. Hsu, X. Jia, S. M. Kim, Y. Shi, M. Dresselhaus, T. Palacios, and J. Kong, "Synthesis and characterization of hexagonal boron nitride film as a dielectric layer for graphene devices," *ACS Nano*, vol. 6, no. 10, pp. 8583–8590, 2012.

[27] M. Ishigami, J. Chen, W. Cullen, M. Fuhrer, and E. Williams, "Atomic structure of graphene on SiO_2," *Nano Letters*, vol. 7, no. 6, pp. 1643–1648, 2007.

[28] K. S. Novoselov, D. Jiang, F. Schedin, T. J. Booth, V. V. Khotkevich, S. V. Morozov, and A. K. Geim, "Two-dimensional atomic crystals," *Proceedings of the National Academy of Sciences of the United States of America*, vol. 102, no. 30, pp. 10451–10453, 2005.

[29] C. Lee, X. Wei, J. Kysar, and J. Hone, "Measurement of the elastic properties and intrinsic strength of monolayer graphene," *Science*, vol. 321, pp. 385–8, Jul 2008.

[30] Y.-M. Lin, C. Dimitrakopoulos, K. A. Jenkins, D. B. Farmer, H.-Y. Chiu, A. Grill, and P. Avouris, "100-ghz transistors from wafer-scale epitaxial graphene," *Science*, vol. 327, no. 5966, p. 662, 2010.

[31] M. K. Yakes, D. Gunlycke, J. L. Tedesco, P. M. Campbell, R. L. Myers-Ward, C. R. Eddy, D. K. Gaskill, P. E. Sheehan, and A. R. Laracuente, "Conductance anisotropy in epitaxial graphene sheets generated by substrate interactions," *Nano Letters*, vol. 10, no. 5, pp. 1559–1562, 2010.

[32] H. I. Rasool, E. B. Song, M. J. Allen, J. K. Wassei, R. B. Kaner, K. L. Wang, B. H. Weiller, and J. K. Gimzewski, "Continuity of graphene on polycrystalline copper," *Nano Letters*, vol. 11, no. 1, pp. 251–256, 2011.

[33] M. Ohring, *Materials Science of Thin Films*. Elsevier Science, 2001.

[34] S. Campbell, *The Science and Engineering of Microelectronic Fabrication*. Oxford series in electrical and computer engineering, Oxford University Press, 2001.

[35] X. Li, W. Cai, J. An, S. Kim, J. Nah, D. Yang, R. Piner, A. Velamakanni, I. Jung, E. Tutuc, S. K. Banerjee, L. Colombo, and R. S. Ruoff, "Large-area synthesis of high-quality and uniform graphene films on copper foils," *Science*, vol. 324, no. 5932, pp. 1312–1314, 2009.

[36] S.-Y. Kwon, C. Ciobanu, V. Petrova, V. Shenoy, J. Bareo, V. Gambin, I. Petrov, and S. Kodambaka, "Growth of semiconducting graphene on palladium.," *Nano letters*, vol. 9, pp. 3985–90, Nov 2009.

[37] P. Sutter, J.-I. Flege, and E. Sutter, "Epitaxial graphene on ruthenium," *Nature materials*, vol. 7, pp. 406–11, Apr 2008.

[38] J. Coraux, A. N'Diaye, C. Busse, and T. Michely, "Structural coherency of graphene on Ir(111)," *Nano letters*, vol. 8, p. 56570, Jan 2008.

[39] H. Rasool, E. Song, M. Mecklenburg, B. Regan, K. Wang, B. Weiller, and J. Gimzewski, "Atomic-scale characterization of graphene grown on Cu(100) single crystals," *Journal of the American Chemical Society*, vol. 133, pp. 12536–43, Aug 2011.

[40] L. Song, L. Ci, H. Lu, P. B. Sorokin, C. Jin, J. Ni, A. G. Kvashnin, D. G. Kvashnin, J. Lou, B. I. Yakobson, and P. M. Ajayan, "Large scale growth and characterization of atomic hexagonal boron nitride layers," *Nano Letters*, vol. 10, no. 8, pp. 3209–3215, 2010.

[41] M. Corso, W. Auwrter, M. Muntwiler, A. Tamai, T. Greber, and J. Osterwalder, "Boron nitride nanomesh," *Science (New York, N.Y.)*, vol. 303, pp. 217–20, Jan 2004.

[42] T. Greber, L. Brandenberger, M. Corso, A. Tamai, and J. Osterwalder, "Single layer hexagonal boron nitride films on Ni(110)," *e-Journal of Surface Science and Nanotechnology*, vol. 4, p. 410413, 2006.

[43] W. Auwrter, H. U. Suter, H. Sachdev, and T. Greber, "Synthesis of one monolayer of hexagonal boron nitride on Ni(111) from b-trichloroborazine $(ClBNH)_3$," *Chemistry of Materials*, vol. 16, no. 2, pp. 343–345, 2004.

[44] Y. Shi, C. Hamsen, X. Jia, K. K. Kim, A. Reina, M. Hofmann, A. L. Hsu, K. Zhang, H. Li, Z.-Y. Juang, M. S. Dresselhaus, L.-J. Li, and J. Kong, "Synthesis of few-layer hexagonal boron nitride thin film by chemical vapor deposition," *Nano Letters*, vol. 10, no. 10, pp. 4134–4139, 2010.

[45] M. Morscher, M. Corso, T. Greber, and J. Osterwalder, "Formation of single layer h-bn on Pd(111)," *Surface Science*, vol. 600, 2006.

[46] A. Goriachko, Y. He, M. Knapp, H. Over, M. Corso, T. Brugger, S. Berner, J. Osterwalder, and T. Greber, "Self-assembly of a hexagonal boron nitride nanomesh on Ru(0001).," *Langmuir: The ACS journal of surfaces and colloids*, vol. 23, pp. 2928–31, Mar 2007.

[47] C. Mattevi, H. Kim, and M. Chhowalla, "A review of chemical vapour deposition of graphene on copper," *J. Mater. Chem.*, vol. 21, pp. 3324–3334, 2011.

[48] C. Oshima and A. Nagashima, "Ultra-thin epitaxial films of graphite and hexagonal boron nitride on solid surfaces," *Journal of Physics: Condensed Matter*, vol. 9, 1997.

[49] K. L. Chavez and D. W. Hess, "A novel method of etching copper oxide using acetic acid," *Journal of The Electrochemical Society*, vol. 148, 2001.

[50] M. Luton, R. Petkovic, and J. Jonas, "Kinetics of recovery and recrystallization in polycrystalline copper," *Acta Metallurgica*, vol. 28, no. 6, pp. 729–743, 1980.

[51] R. Petkovic, M. Luton, and J. Jonas, "Grain size and high-temperature yield strength of polycrystalline copper," *Metal Science*, vol. 13, no. 10, pp. 569–572, 1979.

[52] R. Petkovic, M. Luton, and J. Jonas, "Recovery and recrystallization of polycrystalline copper after hot working," 1979.

[53] R. N. Pease and H. S. Taylor, "The reduction of copper oxide by hydrogen," *Journal of the American Chemical Society*, vol. 43, 1921.

[54] M. Z. Butt, "Effect of hydrogen attack on the strength of high purity copper," *Journal of Materials Science Letters*, vol. 2, 1983.

[55] I. Platzman, R. Brener, H. Haick, and R. Tannenbaum, "Oxidation of polycrystalline copper thin films at ambient conditions," *Journal of Physical Chemistry C*, vol. 112, no. 4, pp. 1101–1108, 2008.

[56] C. Barrett, J. Lytton, and O. Sherby, "Effect of grain size and annealing treatment on steady state creep of copper," tech. rep., DTIC Document, 1965.

[57] J. Wofford, S. Nie, K. McCarty, N. Bartelt, and O. Dubon, "Graphene islands on cu foils: The interplay between shape, orientation, and defects," *Nano letters*, Oct 2010.

[58] T. L. Brown, J. H. Eugene LeMay, B. E. Bursten, and C. J. Murphy, *Chemistry: The Central Science*. Pearson Prentice Hall, 10th ed., 2006.

[59] C. M. A. Brett and A. M. O. Brett, *Electrochemistry: Principles, Methods, and Applications*. Oxford Science Publications, 2005.

[60] P. A. Jacquet, "On the anodic behavior of copper in aqueous solutions of orthophosphoric acid," *Bull. Soc. Chim. France*, vol. 3, 1936.

[61] W. C. Elmore, "Electrolytic polishing," *Journal of Applied Physics*, vol. 10, no. 10, pp. 724–727, 1939.

[62] W. C. Elmore, "Electrolytic polishing. ii," *Journal of Applied Physics*, vol. 11, 1940.

[63] K. K. Kasem and S. Jones, "Platinum as a reference electrode in electrochemical measurements," *Platinum Metals Review*, vol. 52, 2008.

[64] S.-H. Liu, J.-M. Shieh, C. Chen, K. Hensen, and S.-S. Cheng, "Roles of additives in damascene copper electropolishing," *Journal of the Electrochemical Society*, vol. 153, 2006.

[65] S.-C. Chang, J.-M. Shieh, B.-T. Dai, M.-S. Feng, Y.-H. Li, C. H. Shih, M. H. Tsai, S. L. Shue, R. S. Liang, and Y.-L. Wang, "Superpolishing for planarizing copper damascene interconnects," *Electrochemical and Solid-State Letters*, vol. 6, 2003.

[66] J.-M. Shieh, S.-C. Chang, Y.-L. Wang, B.-T. Dai, S.-S. Cheng, and J. Ting, "Reduction of etch pits of electropolished Cu by additives," *Journal of The Electrochemical Society*, vol. 151, 2004.

[67] S. Lee, Y. Chen, and J. Hung, "The investigation of surface morphology forming mechanisms in electropolishing process," *International Journal of Electrochemical Science*, vol. 7, pp. 12495 – 12506, 2012.

[68] S.-C. Chang, "Microleveling mechanisms and applications of electropolishing on planarization of copper metallization," *Journal of Vacuum Science Technology B: Microelectronics and Nanometer Structures*, vol. 20, p. 2149, Sept. 2002.

[69] A. Awad, N. A. Ghany, and T. Dahy, "Removal of tarnishing and roughness of copper surface by electropolishing treatment," *Applied Surface Science*, vol. 256, 2010.

[70] S. Liu, J. Shieh, C. Chen, B. Dai, K. Hensen, and S. Cheng, "Two-additive electrolytes for superplanarizing damascene cu metals," *Electrochemical and Solid-State Letters*, vol. 8, 2005.

[71] R. Egerton, *Physical Principles of Electron Microscopy: An Introduction to TEM, SEM, and AEM*. Springer, 2005.

[72] P. Griffiths and J. De Haseth, *Fourier Transform Infrared Spectrometry*. Chemical Analysis: A Series of Monographs on Analytical Chemistry and Its Applications, Wiley, 2007.

[73] G. Haugstad, *Atomic Force Microscopy: Understanding Basic Modes and Advanced Applications*. Wiley, 2012.

[74] E. Wilson, J. Decius, and P. Cross, *Molecular Vibrations: The Theory of Infrared and Raman Vibrational Spectra*. Dover Books on Chemistry Series, Dover Publications, 1955.